Photoacoustics 31 (2023) 100496

Contents lists available at ScienceDirect

Photoacoustics

journal homepage: www.elsevier.com/locate/pacs

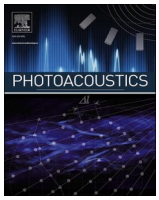

Principles and advances in ultrafast photoacoustics; applications to imaging cell mechanics and to probing cell nanostructure

Bertrand Audoin [1]

University of Bordeaux, CNRS, UMR 5295, I2M, F-33400 Talence, France

ARTICLE INFO

Keywords:
Ultrafast photoacoustics
Basic principles
Recent advances
Applications to cell mechanics

ABSTRACT

In this article we first present the foundations of ultrafast photoacoustics, a technique where the acoustic wavelength in play can be considerably shorter than the optical wavelength. The physics primarily involved in the conversion of short light pulses into high frequency sound is described. The mechanical disturbances following the relaxation of hot electrons in metals and other processes leading to the breaking of the mechanical balance are presented, and the generation of bulk shear-waves, of surface and interface waves and of guided waves is discussed. Then, efforts to overcome the limitations imposed by optical diffraction are described. Next, the principles behind the detection of the so generated coherent acoustic phonons with short light pulses are introduced for both opaque and transparent materials. The striking instrumental advances, in the detection of acoustic displacements, ultrafast acquisition, frequency and space resolution are discussed. Then secondly, we introduce picosecond opto-acoustics as a remote and label-free novel modality with an excellent capacity for quantitative evaluation and imaging of the cell's mechanical properties, currently with micron in-plane and sub-optical in depth resolution. We present the methods for time domain Brillouin spectroscopy in cells and for cell ultrasonography. The current applications of this unconventional means of addressing biological questions are presented. This microscopy of the nanoscale intra-cell mechanics, based on the optical monitoring of coherent phonons, is currently emerging as a breakthrough method offering new insights into the supra-molecular structural changes that accompany cell response to a myriad of biological events.

1. Introduction

Shortly after their development, pulsed lasers were used to generate acoustic waves in liquids or gases, making it possible to analyze the optical absorption spectrum of these media and learn about their composition. Meanwhile, the development of instruments to measure ultrasonic displacements at the surface of reflective materials favored applications that benefited from the possibility of generating and detecting ultrasonic waves without contact and with high spatial resolution. Analysis of the propagation of these acoustic waves has led to the development of laser-ultrasonics, a remote method applied mainly to the non-destructive control and evaluation of solids. In parallel, the absorption of light by biological matter, [1] for example hemoglobin, has made it possible to image vascular networks at depths accessible by the light wave [2]. Using spectroscopic applications of photoacoustics, it is now possible to image specifically addressed exogenous chromophores and to image and characterize the nature of endogenous chromophores [3].

When sufficiently short light pulses are absorbed in a material, the spatio-temporal characteristics of the acoustic waves generated no longer depend on the duration of the pulses. The dynamics are limited temporally by the characteristic times of the energy transfer of the photons towards the medium, typically of the order of a picosecond, and spatially by the volume in which this transfer takes place, currently limited by the optical penetration [4]. Thus, by using the absorption in strongly absorbing media of so-called pump laser pulses, with a duration of less than a picosecond, coherent acoustic waves can be produced, with a very broad spectrum extending to extreme frequencies beyond THz. The detection of a mechanical disturbance on such a bandwidth can, to date, only be done optically using short laser pulses, called probe pulses, to read the transient reflectivity of the medium. Picosecond ultrasonics (PU) is therefore a pump-probe technique that uses a controlled delay between pump and probe pulses to achieve optical sampling of ultrafast transient mechanical response. Developments of the technique have chiefly been driven by research on ultrafast phenomena in the fields of nanoscale solid-state physics. Ultrafast dynamics

E-mail address: bertrand.audoin@u-bordeaux.fr.
[1] https://orcid.org/0000-0003-4632-9883.

https://doi.org/10.1016/j.pacs.2023.100496
Received 5 December 2022; Received in revised form 29 March 2023; Accepted 12 April 2023
Available online 23 April 2023

have mainly been studied in metals, semiconductor or dielectric materials used in sub-micrometric films, multilayered structures and other nanostructures. One major application field of ultrafast photoacoustics is the micro-electronics industry, which requires an accurate means of measuring thicknesses [5–7] and controlling bonding [8–11] and electron transport [12] at a nanometer scale, which the PU technique can provide.

As H. Maris predicted in 1998, in a general article presenting the picosecond ultrasonics technique, [13] the possibility of tackling a variety of applications to the cellular medium quickly emerged. While the first measurements in a liquid, water in this case, were carried out in 2005, [14] the possibility of detecting picosecond acoustic waves in cells was demonstrated in 2008 [15]. Advances in experimental devices then favored the extension to cell imaging, and to the quantitative evaluation of changes in the mechanical properties of cells in response to external biological stimuli.

The purpose of this article is twofold. First, for readers who are not familiar with picosecond acoustics, we describe the foundations of this technique by presenting the main physical phenomena involved. We also introduce some recent advances that have made it possible to push the limits of the field of application. And second we present some of the pioneering and current applications of the technique to the imaging of acoustic properties and to the structural characterization of biological media at the space-scale of picosecond ultrasonics.

The outline of the paper is thus as follows. First we focus on the ultrafast photoacoustic conversion. The basic phenomena are described for the most commonly used materials. Then we present the generation of acoustic waves with transverse polarization, the breaking of the limits imposed by optical diffraction, and the generation of waves guided by interfaces or layers. Next, we introduce the measurement of the dynamic response by means of detecting transient reflectivity changes of the sample. We describe the detection of the acoustic displacement of the interfaces as well as the detection of the acoustic strain during its propagation in an opaque or transparent medium. A section is then dedicated to some of the major advances in experimental devices, which have made it possible to overcome the intrinsic limitations of the original devices and have opened the way to imaging acoustic waves with a better resolution than that limited by optics. Finally, the state of the art concerning the applications of picosecond acoustics to cell mechanics is described briefly. The striking results regarding the demonstration of capabilities for cell imaging and the study of cell nanostructure will be mentioned in the fifth section of this article.

2. Ultrafast photoacoustic transduction

In this section, we describe the physics primarily involved in the conversion of light into high-frequency sound with the help of the main basic equations. For a fuller description of the physical mechanisms of coherent acoustic phonon generation by ultrafast laser action the reader should refer to the review article by P. Ruello et al. [16] Although the interfaces must be considered in most practical cases, for the sake of conciseness, the boundary equations are not stated below, but they can be found in the articles we refer to in this section. In the following the disturbances caused by electron relaxation in metals and by deformation potentials in semiconductors, are presented. Other processes leading to the breaking of the mechanical balance in the medium are also mentioned, for instance those related to changes in molecular conformation in polymer materials. Next, the generation of bulk acoustic shear waves, surface and interface waves, and guided waves is discussed. Finally, we present several instances where the lateral size of the photo-elastic source is smaller than the diffraction limited optical spot size.

2.1. Introduction for metals, the two-temperature model

The emission of coherent acoustic phonon relies on the absorption of light by a material. We begin by describing photoacoustic transduction in a metal half-space with a free surface in the plane $x_1 = 0$ of a Cartesian frame. A pump pulse of duration τ and incident fluence I is focused at a normal incidence on the medium surface on a spot of lateral width χ. Calculation of the electromagnetic Poynting vector in the medium yields the expression of the absorbed energy density:

$$Q(\mathbf{x},t) = \beta I(1-R)g(x_2,x_3)f(t)e^{-\beta x_1} \tag{1}$$

where $g(x_2,x_3)$ and $f(t)$ are Gauss functions of full width at half maximum χ and τ, respectively and β^{-1} is the optical penetration depth in the solid medium. Note that in most experimental situations for metals the spot width is large with respect to the absorption length, suggesting that the energy density is uniform in plane (x_2,x_3) and the problem becomes 1D in space. We now describe how the absorbed electromagnetic energy is partly converted into acoustic waves.

The basic physics of the generation of non-equilibrium coherent acoustic phonon upon the absorption of short light pulses in a solid was described early in the seminal works by Thomsen et al. [4] We consider a general lattice where the mechanical vibrations are with the discrete wave vector $\mathbf{k}$. The absorption of photons modifies the electron and phonon distributions $n_e(\mathbf{k})$ and $n_{ph}(\mathbf{k})$ by $\delta n_e(\mathbf{k})$ and $\delta n_{ph}(\mathbf{k})$, respectively. These equilibrium disturbances deform the lattice and thus produce stress as in:

$$\sigma_{ij} = \sum_{\mathbf{k}} \delta n_e(\mathbf{k}) \frac{\partial E_{\mathbf{k}}}{\partial \eta_{ij}} + \sum_{\mathbf{k}} \delta n_{ph}(\mathbf{k}) \hbar \frac{\partial \omega_{\mathbf{k}}}{\partial \eta_{ij}} \tag{2}$$

where σ_{ij} and η_{ij} are components of the stress and strain tensors, $E_{\mathbf{k}}$ is the energy of an electron and $\omega_{\mathbf{k}}$ the frequency of a phonon of wave vector $\mathbf{k}$. In Eq. 2 $\hbar\omega_{\mathbf{k}}$, with $\hbar$ the Planck constant, is the energy quantum exchanged between a phonon of frequency $\omega_{\mathbf{k}}$ and wave number $\mathbf{k}$ and the crystal. A detailed description of the diffusion and relaxation of the non-equilibrium electrons in metals was given by Gusev et al. [17] The electron-phonon interaction potential ${}^{(2)}\boldsymbol{\gamma}^e$ and the Grüneisen tensor ${}^{(2)}\boldsymbol{\gamma}^l$: [18].

$$\gamma^e_{ij} = -\frac{1}{E_{\mathbf{k}}} \frac{\partial E_{\mathbf{k}}}{\partial \eta_{ij}}, \; \gamma^l_{ij} = -\frac{1}{\omega_{\mathbf{k}}} \frac{\partial \omega_{\mathbf{k}}}{\partial \eta_{ij}} \tag{3}$$

that describe changes in the energy of an electron with respect to the crystal deformation, and changes in the frequency of a vibration mode of a crystal with respect to its volume change, respectively, are introduced in Eq. 2:

$${}^{(2)}\boldsymbol{\sigma} = -\sum_{\mathbf{k}} {}^{(2)}\boldsymbol{\gamma}^e E_{\mathbf{k}} \delta n_e(\mathbf{k}) - \sum_{\mathbf{k}} {}^{(2)}\boldsymbol{\gamma}^l \hbar\omega_{\mathbf{k}} \delta n_{ph}(\mathbf{k}) \tag{4}$$

Assuming thermodynamic equilibrium the electrons and phonons states are described by the Fermi-Dirac and Bose-Einstein distributions, respectively [19]. Eq. 4 is then written with the electron T^e and lattice temperatures T^l as:

$${}^{(2)}\boldsymbol{\sigma} = -{}^{(2)}\boldsymbol{\gamma}^e C^e T^e - {}^{(2)}\boldsymbol{\gamma}^l C^l T^l \tag{5}$$

where C^e and C^l stand for the heat capacity of the electron and the lattice, respectively. Eq. 5 shows that the time and space dynamics of the stress induced by the absorption of photons by the electrons is, in the context of this two-temperature modeling, related to the evolution of the electron and lattice temperatures. Disregarding the thermal dependency of the heat capacities on temperatures, T^e and T^l satisfy a system of coupled linear diffusion equations: [20].

$$C^e \frac{\partial T^e}{\partial t} = \nabla.\left({}^{(2)}\boldsymbol{\kappa}^e \nabla T^e\right) - g\left(T^e - T^l\right) + Q(\mathbf{x},t) C^l \frac{\partial T^l}{\partial t} = g\left(T^e - T^l\right) \tag{6}$$

with ${}^{(2)}\boldsymbol{\kappa}^e$ the tensor of electronic heat conductivity, g the coupling constant and $Q(\mathbf{x},t)$ the source term corresponding to the absorption of the incident photons by the electrons, Eq.1. Note that in Eq. 6 the

diffusion of the thermal phonon was disregarded for simplicity. The electrons absorb the energy of the photons in characteristic time typically less than a picosecond [21] and the over heated electron transfer their energy to the lattice. The lattice absorbs the energy of electrons in characteristic time $\tau^l = C^l/g$ through electron-phonon collisions. This rise-time of the lattice temperature is typically of the order of ≈ 5 ps.

The sudden heating generates transient acoustic displacement, solution of the following wave propagation equation:

$$\rho\frac{\partial^2\mathbf{u}}{\partial t^2} - \nabla.\left({}^{(4)}\mathbf{C} : {}^{(2)}\nabla_s\mathbf{u}\right) = -{}^{(2)}\boldsymbol{\lambda}\nabla T^l - {}^{(2)}\boldsymbol{\gamma}^e C^e \nabla T^e \tag{7}$$

where ρ stands for the mass density, $\mathbf{u}$ is the displacement vector at any position and time, and ${}^{(4)}\mathbf{C}$ denotes the fourth order stiffness tensor. ${}^{(2)}\boldsymbol{\lambda} = {}^{(4)}\boldsymbol{C} : {}^{(2)}\boldsymbol{\alpha}$ is the thermal rigidity tensor in which ${}^{(2)}\boldsymbol{\alpha}$ is the thermal expansion tensor [22]. The second term on the right in Eq. 7 is the contribution of the fast electron dynamics to the acoustic source. Thus the upper limit of the frequencies generated by this electronic expansion, $1/\tau^e$, is higher than THz. The rise-time τ^l of the lattice temperature limits the range of frequencies generated by the macroscopic expansion of the source. This influence of the lattice temperature on thermoelastic generation appears in the first term on the right in Eq. 7. The dynamics of waves induced by the photo-elastic expansion can also be limited by the source volume of which the smallest characteristic size is generally along depth, Eq. 1, with an optical penetration depth in metals of ≈ 10 nm or less. This source size can be increased by fast diffusion of over-heated electrons over a distance of $(\kappa^e_{11}/g)^{1/2}$ because electrons may diffuse across a significant distance before they lose their energy. This can lead to a limitation to reach frequencies in the THz range, which can be overcome by using thin-layered structures to achieve the transduction [23]. Thus, for a large number of experimental situations, and especially when acoustic frequencies in the GHz range are sought, one can assume that macroscopic equilibrium is reached instantaneously and the evolution of the temperature T, and thus of the source term in the wave equation, is merely governed by a parabolic heat diffusion equation:

$$\rho C_p\frac{\partial T}{\partial t} - \nabla.\left({}^{(2)}\boldsymbol{\kappa}\nabla T\right) = Q(\mathbf{x},t) \tag{8}$$

where C_p denotes the specific heat and ${}^{(2)}\boldsymbol{\kappa}$ is the thermal conductivity tensor [22].

These assumptions, and consequently this equation, are widely used in the literature. The macroscopic heat diffusion in Eq. 8 generally yields an asymmetry [24] of the acoustic pulses, and it can also be disregarded for qualitative descriptions of the acoustic transients. One can also note that the dissipation of ultrafast particle motion could yield heat sources in the right-hand side in Eq. 8, but which are negligible in experiments performed at room temperature.

2.2. Opto-acoustic transduction in semi-conducting materials

A non-thermal and efficient generation process takes place in semiconducting materials when the energy E of each incident photon is greater than the semiconductor energy band-gap E_g. Electrons are then extracted from the valence band of the crystal to the conduction band, and electron-hole pairs are generated. For simplicity we do not dissociate the dynamics of electrons and holes. The time and space dependency of plasma density N is governed by the electron diffusion and by non-radiative electron-hole recombination. Assuming that Auger recombination is the dominant recombination mechanism, the corresponding diffusion equation is: [25].

$$\frac{\partial N}{\partial t} - \nabla.\left({}^{(2)}\boldsymbol{\Lambda}\nabla N\right) + \frac{1}{\tau_R}N = \frac{Q(\mathbf{x},t)}{E} \tag{9}$$

Here ${}^{(2)}\boldsymbol{\Lambda}$ stands for the ambipolar carrier diffusion tensor. In Eq. 9, the non-radiative Auger recombination is taken into account by the third term in the left-hand side. There, τ_R represents the lifetime of charge carriers, the so-called Auger recombination time. Since recombination occurs over a long time-scale (ns-μs) this term can be ignored in the plasma diffusion equation, Eq. 9, when short time-scale dynamics are studied [24,26]. The right-hand side of Eq. 9 describes the photo-generation of charge carriers; it expresses that each photon creates one electron-hole pair. Note that the interaction of temperature or phonons with charge carrier density is ignored in this equation. Note also that for the same reason as in metals, the diffusion of charge carriers may result in broadening of the acoustic response [27].

The temperature rise results from both opto-thermal and opto-electronic effects. It satisfies the following diffusion equation:

$$\rho C_p\frac{\partial T}{\partial t} - \nabla.\left({}^{(2)}\boldsymbol{\kappa}\nabla T\right) = \left(E - E_g\right)\frac{Q(\mathbf{x},t)}{E} + \frac{E_g}{\tau_R}N \tag{10}$$

As already mentioned, each photon brings one electron from the valence band to the conduction band. It immediately drops to the minimum of the conduction band. The energy released for thermalization is then $E - E_g$. The first term in the right-hand side of Eq. 10 therefore quantifies the amount of incident energy that is directly thermalized. The last term describes crystal heating from the energy released by the charge carriers that recombine during Auger time. The left-hand side of Eq. 10 is similar to that of the classical parabolic Fourier diffusion equation but the hyperbolic diffusion equation in either of its form could be preferred [28].

The acoustic wave equation accounting for thermoelastic and electronic deformation mechanisms, is written as:

$$\rho\frac{\partial^2\mathbf{u}}{\partial t^2} - \nabla.\left({}^{(4)}\mathbf{C} : {}^{(2)}\nabla_s\mathbf{u}\right) = -{}^{(2)}\boldsymbol{\lambda}\nabla T - {}^{(2)}\mathbf{D}\nabla N \tag{11}$$

The coupling between plasma density and stress is introduced by mean of the tensor of electroacoustic coupling ${}^{(2)}\mathbf{D} = {}^{(4)}\boldsymbol{C} : {}^{(2)}\mathbf{d}$, [29] accounting for the difference in deformation potential of the conduction and valence bands. Parameter ${}^{(2)}\mathbf{d}$ quantifies the changes with stress of the band gap energy E_g. The components for tensor ${}^{(2)}\mathbf{d}$ are:

$$d_{ij} = -\frac{\partial E_g}{\partial \sigma_{ij}} \tag{12}$$

The contributions from the two source terms in the right-hand side in Eq. 11 may have different signs. Usually, the temperature rise produces a negative stress, whereas the electronic strain caused by carriers diffusion can be of either sign. For instance, it can be positive for silicon thus electronic strain produces contraction. For suitable pump wavelength and fluence this strain can be larger in absolute value but with opposite sign than the thermal strain. It results to an overall contraction of silicon upon pump absorption [26,30].

2.3. Other physical mechanisms allowing light conversion into acoustic short pulses

A variety of physical mechanisms allowing photoacoustic transduction have been reported in the literature. Along with the above-mentioned photo-elastic coupling, driven by hot carriers and electronic deformation potential, other mechanisms have been revealed. Piezoelectric coupling can be the dominant generation process in materials - semiconductors, [31] ferroelectrics [32] - where the presence of built-in electric fields allows the efficient generation of acoustic waves due to the laser-induced inverse piezoelectric effect. It accompanies the spatial separation of electrons and holes following absorption of optical radiation in piezoelectric semiconductors. In addition, electrostriction was notably shown to be efficient as a phonon generation mechanism in polymers in the glassy state and in liquids [33,34].

Although experiments with *cis*-polyacetylene were reported in the pioneering article in 1984 by Thomsen et al. [4] the opto-acoustic

transduction in polymers has not been studied much since. However, the possibility of obtaining efficient transduction with polymers containing chromophores was investigated recently. In addition to the thermal expansion resulting from electron relaxation, efficient film deformation can be expected if polymers are selected with an absorption band, for a *cis-trans* isomerisation, that matches the pump laser wavelength. In this regard, the use of an azo group was shown to be very promising. Large reversible thin film deformation was obtained by inducing photochemical *trans-cis* isomerization under UV irradiation in azobenzene [35,36]. The change in shape between the *cis* and *trans* conformation requires an increase in the free volume of the polymer matrix. These volume changes have been observed on the picosecond time scale, on which molecular rearrangement takes place, using nano-scale azo-compound materials [37]. The low acoustic impedance of such a polymer transducer shows great promise for improving acoustic transmission in studying soft matter objects in general and for picosecond cell ultrasonography in particular.

2.4. Seeking shear waves

The laser generation of picosecond acoustic waves in opaque thin films is generally considered as a one-dimensional problem because the size of the laser spot, typically microns, is large with respect to the sample thickness, thus experiments are carried out in the acoustic near field; and in this near field, the source directivity is great because this spot size is much greater than the acoustic wavelengths in play. Therefore, a single phonon wave vector direction is considered, and it is along the normal to the interface where optical absorption occurs underneath. Thus, for isotropic media, these experiments address only one of the acoustic polarizations, the longitudinal one.

However, generation of the shear wave would also greatly extend the field of picosecond laser ultrasonics. For instance, for an isotropic medium where the two shear modes are degenerated one would access both the shear and tensile stiffness, and the relaxation dynamics. Also, the shear wave velocity is lower, particularly for soft matter, leading to a shorter wavelength for a given frequency which would be advantageous for nanoscale probing.

The above-mentioned limitations can be overcome in two main ways. Firstly, the one-dimensional character can be broken, still with a phonon wave vector along a single direction, when the symmetry of the physics involved in the generation is somehow broken. For this, anisotropic materials are very helpful. When the absorbing material is anisotropic, with principle axes of symmetry off the sample interface, the photothermal relaxation may yield shear stresses. Whether it does or not, thermal dilatation launches both quasi-longitudinal and quasi-transverse waves in the anisotropic opaque material as they are coupled when the wave vector is off the crystal principle axis of symmetry [38,39]. Such anisotropy was proven beneficial to quasi-shear waves generation when the photo-elastic transduction was achieved with the inverse piezoelectric effect [40] or in ferroelectric materials [41]. Still benefitting of the symmetry breaking with anisotropy, quasi-shear waves can also be obtained using an isotropic absorbing transducer in contact with a transparent crystal. With the normal to the interface off the transparent crystal axis of symmetry, refraction of the longitudinal phonon at the absorbing transducer-transparent crystal interface allows transmission of quasi-longitudinal and quasi-transverse waves with their relative amplitude depending on the crystal orientation with respect to the interface [42]. Note that for all the above cases, the Poynting vector of the quasi-shear waves lies off the normal to the interface and the projection of their group velocity along this normal equals the phase velocity.

Secondly, by reducing the width of the laser spot on the surface, the opto-acoustic source is less directive and, because of the presence of the surface, pure shear waves can be diffracted in an isotropic half-space in the far field of the acoustic source [43,44]. If the generation was achieved in a film, reflection at the interfaces is either with or without mode conversion, and successive echoes of waves propagating back and forth through the plate provide observation of the acoustic field at increasing travel distances from the source. From the near field to the far field, amplitude of the shear wave increases. However, as the spot focusing is limited by optical diffraction, with pump wavelength in the visible range, acoustic diffraction is efficient mainly in the lower side of the hypersound frequency spectrum. The shear wave amplitude can be magnified by measuring signals for several respective pump-probe distances and using delay and sum methods [45,46]. Diffraction of the shear wave was also observed in thick anisotropic samples and their frequency was controlled by patterning the sample surface with dots of various sizes and resonance frequencies [47].

2.5. Surface and guided waves

By focusing the pump and probe spots at a distance along a medium surface, the surface waves propagating along this surface can be measured. Because the wavelength of surface waves is basically monitored by the size of the optical spot the frequencies are generally limited to ≈ 1 GHz, although surface waves at ≈ 10 GHz have been detected at the free surface of highly ordered polygraphite micro-layers [48]. This limitation can however be overcome using nanostructures etched on the sample surface and by exploiting the plasmon-polariton resonances of the nanostructures for the acousto-optic detection [49,50].

To illustrate the wide variety of potential uses of the GHz surface acoustic waves, let us mention just a few of their applications. The complete elastic characterization of a medium, both longitudinal modulus and Poisson's ratio, was possible by recording the skimming longitudinal and the Rayleigh wave propagating along the surface [51]. Regarding inhomogeneous materials, grains orientation was determined by mapping the refraction of surface waves through the interface between crystallites on the surface of a sample [52]. The micro-patterning of two-dimensional phononic crystals on the sample surface has permitted demonstration of the mastering of phonon propagation on the surfaces. It enabled, for instances, the observation of caustics, [53] of negative refraction, [54] or the guiding of ultrasound waves along micron guides in rows of lacunas in two-dimensional phononic crystals [55].

Measurement of the dispersion of guided waves propagating in free-standing [56] and sustained [57] films of sub-micron thickness was demonstrated. Guided waves in general and zero-group velocity (ZGV) Lamb waves in particular are highly sensitive to thin layer thicknesses, material elastic constants, notably Poisson's ratio, and interfacial stiffness between bonded layers. ZGV were measured at GHz frequencies with Q factors of $\approx 10^3$ in a silicon-nitride plate coated with a titanium film [58].

The generation of surface and guided waves is favored when the shape of the pump laser spot on the sample surface is not a disc but made instead of periodically spaced optical lines, thus concentrating most of the input energy into controlled phonon wave vectors along one direction on the surface. Suitable transient gratings can be obtained by shaping the pump pulses with optical masks, creating two-beam interference on the surface, or by using electrically-addressed spatial light modulators [59,60]. This technique was used to characterize thin liquid and solid films and it could also be used to generate bulk shear waves [61].

2.6. Breaking the optical diffraction limit

The above-mentioned results were achieved by converting the light pulses in coherent acoustic phonons thanks to the absorption of pump pulses in the medium of interest or in an adjacent medium. Acoustic phonons are launched in the direction normal to the interface with wavelength defined by optical penetration and, if applicable, by hot carrier diffusion. These wavelengths are much smaller than optical wavelengths thus providing outstanding capability for in-depth space

resolution. The lateral extent of the opto-acoustic source is however restricted by light focusing, and hence by the optical diffraction limit. This places limitations on the in-plane imaging resolution, limits the capability for acoustic diffraction, and bounds the upper frequencies of the generated surface and interface waves.

This optical diffraction limit was overcome using scanning near-field optical microscopes (SNOM). In SNOM, a single mode fiber tip is pulled down to a diameter of ≈ 100 nm and coated with aluminum. A lateral resolution of that size was demonstrated for photothermal and for photoacoustic imaging. The technique however requires the fiber tip to be brought very close to the sample surface, within 10–20 nm [62,63].

Alternatively, picosecond ultrasonic experiments were carried out with a similar saturation technique to the stimulated emission depletion used for fluorescence imaging [64]. As mentioned above, transient strain is produced in piezoelectric materials due to the screening of a built-in piezoelectric field by photo-excited charge carriers. For a large carrier density the screening field produced by the photo-carriers can be larger than the built-in piezoelectric field and then, saturation occurs. A pre-injection laser pulse is then used to produce a dense doughnut-shaped carrier distribution. The diffraction-limited pump pulse is then injected and produces higher strain at the center of the doughnut where the screening is not saturated. With this technique acoustic waves could be generated with a spot size of ≈ 100 nm in the optical far field [65].

2.7. *Indirect transduction: use of optically excited nanostructures to launch acoustic waves in the supporting or surrounding medium*

Using pump-probe set-ups it is possible to detect vibrational modes of various confined single nano-objects whose frequencies are in the range reachable in PU experiments and to assess the elastic properties of the nano-objects. A review of ultrafast spectroscopy of the vibrational landscape of single nanoparticles can be found for instance in Ref [66]. Interestingly, absorption of pump pulses by the nano-objects can excite vibrational modes that couple with the supporting or surrounding medium and then launch acoustic phonons that propagate in this medium.

With two-dimensional phononic crystals made of aluminum nano-cube lattices on an aluminum under-layer, collective modes resulting from the coupling between cubes inside the crystal were excited using ultrafast acoustics [67]. These modes can be at lower frequencies than individual resonances of the cubes and result from the displacement of one object with respect to the other, similar to an acoustic phonon in an atomic crystal. They yield information on the propagation of guided acoustic waves along the under-layer at frequencies up to ≈ 8 GHz, greater than that accessible with a pump focused on the aluminum film free of nano-cubes.

Rayleigh surface acoustic waves at frequencies of several GHz were generated with a one-dimensional array of absorbing nanostructures [68]. This consisted of equally spaced gold nano-lines of sub-micron lateral sizes deposited on a transparent substrate. This geometry provides a sharp directional response and reduced amplitude decrease by geometrical scattering. It is thus promising for sensing applications of molecular adsorption between lines, for instance. Going deeper into miniaturization, the generation of Rayleigh surface waves at ≈ 10 GHz by light absorption in a single line with sub-100 nm lateral sizes was demonstrated recently [50].

Bulk acoustic waves can also be emitted in the supporting medium from the light-absorbing nanostructure. To this aim, gold discs of a diameter down to 0.3 μm were lithographed on a 160 μm thick silicon substrate. Focusing the pump beam on a single disc provides efficient transduction and bulk longitudinal and shear waves at a frequency of ≈ 3.5 GHz could be detected at the silicon plate surface opposite to that where the disc was lithographed. The opposite surface was coated with a metal film to optically detect the transient arrivals [47]. Recently, acoustic waves generated by optical absorption in a single copper nanowire in contact with the surface of a 10 μm thick silicon membrane were detected on the rear metallized side of the membrane [69]. However, the propagation of coherent acoustic phonons along their path from a nano-optoacoustic transducer can be detected in a transparent material through the acousto-optic interaction [70]. A single gold nanorod dropped on the surface of a silica substrate was used as an acoustic source. Acoustic eigen modes of the nanorod at GHz frequencies are then optically excited on a picosecond time-scale. A part of the eigen mode energy is transmitted to the substrate through the nanorod-substrate contact. The acoustic wave generated in this way produces a refractive index perturbation in the substrate that propagates at the acoustic velocity in the supporting medium. As presented below, a coherent phonon whose frequency matches the Brillouin frequency shift f_B can then be detected along their propagation length in a time-resolved fashion. For a probe wavelength of 750 nm their frequency is 23 GHz in silica. When the breathing mode of the nanorod matches this frequency, which occurs for a gold nanorod diameter of ≈ 50 nm, the sample reflectivity reveals large phonon-photon interaction. Phonons generated by the nanorod, of wavelength of 260 nm, were detected in silica up to a depth of ≈ 20 μm. Interestingly, the maximum in the reflectivity signal is not at the beginning of the signal, as observed when phonon are excited by an impulsive opto-acoustic source, but occurs after a certain delay, see Fig. 6 in Ref. [70]. The rise-time of the reflectivity signal fits the lifetime of the excited eigen mode of the nanorod revealing the energy transfer from the nanorod surface vibrations toward the acoustic wave detected in silica.

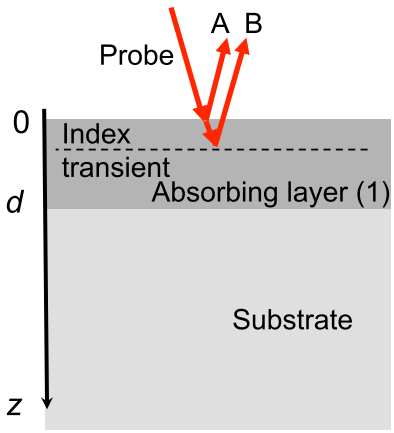

Fig. 1. Reflection of the probe pulse at the surface of an absorbing layer.

3. Detection

In this section, we describe the detection of the coherent acoustic phonon with probe light pulses. Again, the very basics are described with simple equations without going into details of their derivations which lead to representations of the experimental results. For a more in-depth description of detection in picosecond ultrasonics, the reader should refer to the review articles by Matsuda et al. [71] and Gusev et al. [72].

3.1. *Changes in optical reflectivity of an absorbing sample*

We consider the simple one-dimension problem of the probe beam at normal incidence to the sample surface. The sample, medium 1, is first modeled as an optically and mechanically isotropic layer of thickness d, see Fig. 1. It is made of a material, e.g. a metal, that strongly absorbs the probe light, $k''_1 > k'_1$, where k'_1 and k''_1 are real and imaginary parts of the probe wavenumber, respectively, and the layer thickness is greater than the probe penetration depth, $2k''_1 d >> 1$. This is a standard situation where the absorption of a pump pulse at the sample surface has induced acoustic pulses that partly reflect at the layer-substrate interface

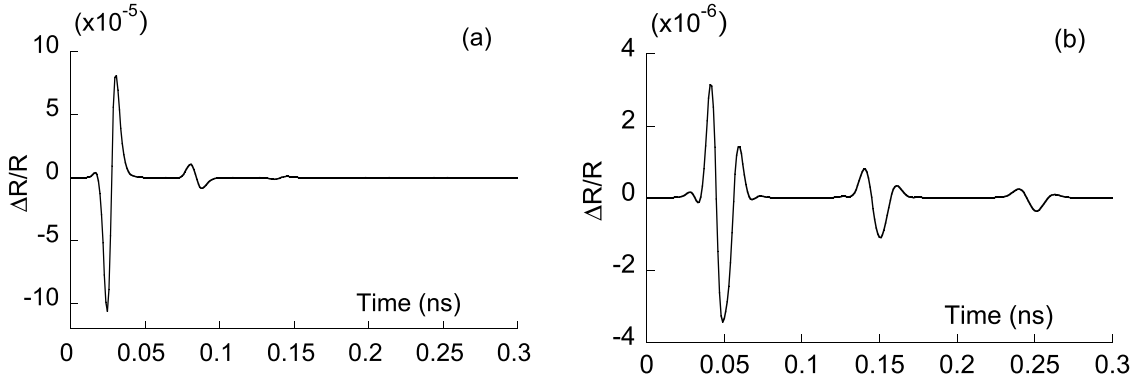

Fig. 2. Relative changes in reflectivity calculated with pump focused at the substrate-layer interface and with the probe at the free surface of a metal film of thickness 200 nm on a substrate. (a) titanium film on sapphire and (b) tungsten film on silica.

and are bouncing back and forth through the layer.

Let r_{01} be the reflection coefficient for the probe at the sample surface at rest. After absorption of the pump pulse, probe reflection is perturbed firstly because of the displacement $u_1(0,t)$ of the sample free surface caused by thermal dilatation and acoustic displacement. It leads to a change in phase of the probe light reflected at the free surface, shown with label A in Fig. 1. As the displacement is small with respect to the probe wavelength, the probe reflection disturbance caused by the surface motion can be linearized as:

$$\delta r_A(t) = 2jk_0 r_{01} u_1(0,t) \tag{13}$$

where k_0 stands for the probe wavenumber in vacuum.

Secondly, the sample reflectivity changes because the refractive index below the surface is sensitive to changes in temperature and to acoustic strain. Because local perturbation of the refractive index, shown schematically with a dashed line in Fig. 1, is small one can consider that it depends linearly on strain $\eta_1(z,t)$ and on temperature changes $T_1(z,t)$ as:

$$\delta n_1(z,t) = \frac{\partial n_1}{\partial \eta_1}\eta_1(z,t) + \frac{\partial n_1}{\partial T_1}T_1(z,t) \tag{14}$$

where $\partial n_1/\partial \eta_1$ and $\partial n_1/\partial T_1$ denote the complex photo-elastic and photothermal constants at probe wavelength, respectively. The small reflection of light, locally at the sample transient is:[24].

$$r_\delta = jk_0 \delta n_1(z,t) \tag{15}$$

As we are interested in detecting the acoustic transients, we disregard the contribution of the temperature rise to the disturbance of the refractive index. Thus, integrating along the depth one obtains changes in sample reflectivity caused by strain:

$$\delta r_B(t) = jt_{01}t_{10}k_0 \frac{\partial n_1}{\partial \eta_1}\int_0^d \eta_1(z,t)e^{2jk_1 z}dz \tag{16}$$

where t_{01} and t_{10} stand for transmission coefficients at the vacuum-sample and sample-vacuum interfaces, respectively. For absorbing materials, which we are considering in this section, the integral in Eq. 16 is small because strain is null at the free surface of the sample and because the integral is along the skin depth only. This especially holds when the acoustic wavelengths are large with respect to the optical penetration depth, as is the case with photoacoustic experiments in the MHz range. Then the phase of the reflection coefficient depends on $\delta r_A(t)$ only, Eq. 13, and optical interferometers allow for the direct measurement of the surface acoustic displacement $u_1(0,t)$ or of its velocity [73,74]. We will discuss in the next section measurement of the phase of the reflection coefficients with optical interferometers in picosecond ultrasonic experiments.

The changes in the reflected light intensity are, at first order,

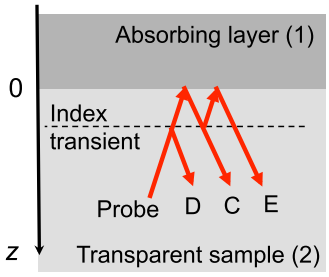

Fig. 3. Changes in optical reflectivity of a transparent sample.

$\Delta R \approx 2Re[r_{01}{}^* \delta r_B(t)]$, not dependent on $\delta r_A(t)$. Acoustic pulses that may propagate back and forth through the layer are thus revealed by the integral of strain along the skin depth, Eq. 16. Many different situations have been documented in the literature. To illustrate this we show in Fig. 2 the relative changes in the reflectivity of the metal film on substrate, Fig. 1, calculated with the physical parameter given in appendix, and assuming the pump is focused at the substrate-layer interface with a fluence of $I = 160\,\mu J/cm^2$. For this opposite pump and probe focusing and for such thickness of the metal layer, i.e. 200 nm, the thermal contribution to the changes in reflectivity, Eq. 14, can be disregarded. When the acoustic impedance of the transparent substrate is greater than that of the absorbing film, as for titanium on sapphire, Fig. 2(a), the strain pulse generated by light absorption is mono-polar. It is detected along skin depth at the free surface of film before and after its reflection at the mechanically free surface. This gives the bipolar shape of the reflectivity changes. The following acoustic echoes are of less magnitude and π-shifted owing to the successive reflections at the free surface. Amazingly, for the reverse case where the acoustic impedance of the transparent substrate is less than that of the absorbing film, as for tungsten on silica, the strain pulse generated by light absorption is bi-polar. This yields the more intricate shape of the detected reflectivity changes shown in Fig. 2(b). The successive echoes have decreasing amplitude but are not π-shifted because the reflection coefficient for strain is negative also at the film-substrate interface.

3.2. Changes in optical reflectivity of a transparent sample

Next, we consider a usual situation, Fig. 3, where a transparent sample, medium (2) such that $k''_2 << k'_2$, is in contact with an absorbing material, medium (1) where the pump light absorption launches acoustic pulses that are transmitted to the transparent material. The probe light is assumed incident at the transparent-absorbing medium interface, Fig. 3, and the transparent sample is considered as a semi-infinite medium, i.e. its thickness is larger than the probe pulse length, typically 30 μm for 100 fs pulse duration. The origin for the phase is at

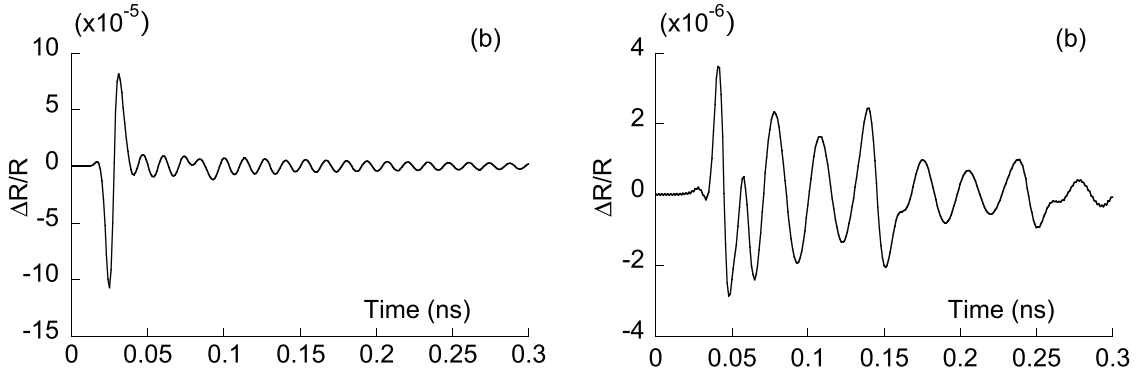

Fig. 4. Relative changes in reflectivity calculated with pump at the free surface of metal film and probe at the interface between transparent substrate and metal film of thickness 200 nm. (a) titanium film on sapphire and (b) tungsten film on silica.

the interface. The following description of the changes in the sample reflectivity was first given by Lin et al. [75].

Changes in the probe's reflectivity are caused firstly by changes in the reflectivity of the absorbing layer (1) caused by strain and heating in this material. This can be described along the same lines as mentioned in the previous section, thus it will not be mentioned further. Rather, we set out the changes in probe reflectivity in relation to the acousto-optic effect in the transparent medium (2).

Let r_{21} be the reflection coefficient of the probe at the transparent-absorbing material interface. The probe light reflected at the interface, shown with label C in Fig. 3, is transmitted twice through index transient thus its reflection coefficient is $r_{21}(1+r_\delta)^2 \approx r_{21}(1+2r_\delta)$. The reflectivity change caused by strain is therefore:

$$\delta r_C = 2jr_{21}k_0\frac{\partial n_2}{\partial \eta_2}\int_0^{+\infty}\eta_2(z,t)dz \tag{17}$$

where $\eta_2(z,t)$ and $\partial n_2/\partial \eta_2$ denote strain and photo-elastic constant in the transparent medium (2), respectively. Thus this change provides information on the displacement $u_2(0,t)$ of the interface as:

$$\delta r_C = -2jr_{21}k_0\frac{\partial n_2}{\partial \eta_2}u_2(0,t) \tag{18}$$

or of changes in the thickness of the transparent sample if it was finite [76].

Following the same steps as for the calculation of $\delta r_B(t)$, Eq. 16, it is straightforward to derive the integral expressions for δr_D and δr_E:

$$\delta r_D = jk_0\frac{\partial n_2}{\partial \eta_2}\int_0^{+\infty}\eta_2(z,t)e^{-2jk_2z}dz,\ \delta r_E = jr_{21}{}^2k_0\frac{\partial n_2}{\partial \eta_2}\int_0^{+\infty}\eta_2(z,t)e^{2jk_2z}dz \tag{19}$$

In view of the integrals in Eq. 19 it is tempting to substitute strain by its integral Fourier transform in space. After some calculations, one obtains:

$$\delta r_D = -2j\pi k_0\frac{\partial n_2}{\partial \eta_2}\widetilde{\eta}_2(q=2k_2,t),\ \delta r_E = -2j\pi r_{21}{}^2k_0\frac{\partial n_2}{\partial \eta_2}\widetilde{\eta}_2(q=-2k_2,t) \tag{20}$$

Eq. 20 shows that δr_D and δr_E are commensurate with the Fourier component of strain for phonon wavenumbers $q=2k_2$ and $q=-2k_2$, respectively. It refers to the conservation of momentum and shows that δr_D and δr_E result from the anti-Stokes or the Stokes Brillouin scattering, respectively. This resulted from the calculations because of the phase shifts in the integrands in Eq. 19, see Fig. 3. However, when r_{21} is weak, the anti-Stokes interaction contributes mainly to reflectivity changes.

The relative changes in reflected light intensity, which do not depend on the incident probe intensity, are:

$$\frac{\Delta R}{R} = \frac{1-|r_{21}|^2}{|r_{21}|}4\pi k_0\frac{\partial n_2}{\partial \eta_2}|\widetilde{\eta}_2(q=2k_2,t)|sin(2k_2z+\varphi+\psi) \tag{21}$$

where φ is the argument of the reflection coefficient r_{21} and ψ is that of $\widetilde{\eta}_2(q=-2k_2,t)$. It is worth noting that for a perfectly reflecting interface the above change in light reflectivity is null, no such Brillouin oscillations are detected [75].

Keeping in mind that z denotes the position of the acoustic wavefront, propagating at sound velocity V, $\Delta R/R$ is an oscillating signal at frequency $f_B = 2n_2V/\lambda$. To illustrate this, in Fig. 4 we plotted the relative changes in the intensity of the reflected light calculated for the probe beam focused at the substrate-metal interface, and assuming the pump is focused at the free surface of the film for the same materials as for Fig. 2. The acoustic echoes bouncing back and forth through the film are visible owing to the probe penetrating the metal film. The acousto-optic contribution in the transparent medium, Eq. 21, is overlaid showing so-called Brillouin oscillations in the time domain. Their respective amplitude depends on acoustic transmission at the film-substrate interface, the optical reflection coefficient at the substrate-film interface and the piezo-optic coefficients. These oscillations are at the frequency of the Brillouin shift, typically 7.9 GHz in water, [77] 34 GHz in silica, [78] and 77.4 GHz in sapphire [98] with probe wavelength of 512 nm.

The measurement of this frequency for several probe wavelengths has been used to probe the sample mechanics, both elasticity and dissipation, for a large bandwidth in the GHz frequency range [79]. Moreover, as the Brillouin frequency shift can be measured in a time-resolved fashion using the PU technique it becomes possible to measure sound velocity locally with a theoretical in-depth resolution of half the optical wavelength, thus allowing notable applications to depth profiling [72].

3.3. Changes in optical reflectivity of a multi-layered sample

When thickness of the transparent material (2), Fig. 2, is less than the probe pulse length the interface between vacuum and medium (2) plays an important role in the detection mechanism. Because of the internal reflection of probe light at this interface, it will introduce additional interactions of the probe light with the acoustic wave front. Moreover, an optical cavity is built which the transmission coefficient will infer on the sensitivity to changes in the reflectivity of the absorbing layer (1) caused by strain and heating in this material. Finally, the reflectivity of the optical cavity strongly depends on its length therefore to the periodic displacement of the interfaces caused by acoustic pulses bouncing back and forth in the layer. This introduces a periodic modulation of the recorded time-trace [80,81].

From the considerations above it appears that prediction of the reflectivity changes caused by strain in a stacking of transparent and

partly absorbing layers can be complex and difficult to handle. Analytical descriptions, accounting for contributions from surface and interface motion as well as changes in refractive index in the bulk of the layers were proposed based on the transfer matrix method for propagation of the electromagnetic and acoustic fields[82,83]. Derivation of the Green function provided a compact formalism that could be used to predict light disturbance in an arbitrary multi-layered structure subject to an inhomogeneous perturbation in its dielectric constants [82].

Multi-layered structures can constitute super-lattices of increasing interest because of the outstanding behavior one may expect while coupling photonic and phononic nano-structures. Progresses and applications of these structures will however not be treated in this manuscript.

3.4. Oblique photon-phonon interaction and shear wave detection

When wave-vectors of the interacting photon and phonon are not in the same direction but instead lie at an angle, as occurs for instance when probe light is at a non-normal incidence with respect to the interface where coherent phonons are generated, then the wavelength of probed phonons can be controlled with the angle. Notably, measurement of changes in the Brillouin frequency with the incidence angle has made possible the reconstruction of the strain profile, [84] or the measurement of both the sound velocity and refractive index in a single run experiment [72].

Importantly, in these situations where coherent acoustic phonons and probe photons are at an angle, the one-dimensional description, on which the previous sub-section relies, does not hold. Nor would this description suit for general directions of the transparent material, if it were birefringent. Thus perturbation of the refractive index by strain is no longer described by the simple Eq. 14. Instead, one must account for the more general linear relationship between the perturbation of the second order permittivity ${}^{(2)}\delta\boldsymbol{\varepsilon}(\mathbf{x},t)$ tensor at any position $\boldsymbol{x}$ in space, and the strain ${}^{(2)}\boldsymbol{\eta}(\mathbf{x},t)$ tensor:

$$ {}^{(2)}\delta\boldsymbol{\varepsilon}(\mathbf{x},t) = {}^{(4)}\mathbf{P} : {}^{(2)}\boldsymbol{\eta}(\mathbf{x},t) \tag{22}$$

where ${}^{(4)}\mathbf{P}$ stands for the fourth order photo-elastic tensor. For symmetry reasons, the scalar components of ${}^{(4)}\mathbf{P}$ depend on only two independent parameters in the case of an isotropic material. This relation allows one to describe the perturbation of the electromagnetic properties of the medium by an acoustic disturbance and thus deduce how the electromagnetic wave will be changed in terms of amplitude, phase and polarization. Calculations, not given here, would illustrate that the acoustic shear wave cannot be detected in an isotropic material if photon and phonon wave vectors lie in the same direction. Conversely, the oblique interaction that supports the reflectivity changes allowing detection of shear waves has been fully described for plane [38,85] and divergent [86] wavefronts in transparent and absorbing materials. As the acoustic strain can induce transient anisotropic perturbation of the refractive properties of the transparent material, Eq. 22, polarization of the probe light reflected by the sample can change. Thus transient femtosecond ellipsometry has shown great sensitivity to the acoustic strain, notably that associated with shear strain pulses [87–89].

4. Some instrumental advances

In this section we describe the basic features of the experimental setup and mention several advances in the field that have resulted in the initial limitations being overcome. While interferometric detection has been implemented rapidly and has been steadily improved, recent advances in devices make it possible to significantly improve the time required to perform the optical sampling of the transient response, to concentrate the frequency spectrum of the phonons generated and improve the spectral resolution, and also to drastically improve the spatial resolution for imaging applications.

The PU technique is based on a time-resolved pump-probe setup using ultra-short laser pulses as delivered, for instance, by a Ti:Sa laser. For such a laser, typical wavelength, pulse duration, energy per pulse and repetition rate are basically 780 nm, 100 fs, 10 nJ, $f_1 = 78$ MHz, respectively. The probe pulse is delayed with respect to the pump pulse, up to a few nanoseconds with a temporal accuracy of a few tens of femtoseconds by means of a variable and mechanically controlled optical path. To improve the signal to noise' ratio, the pump beam, for which the length of optical path remains constant during the experiment, is modulated at a given frequency f_2, with $f_2 < f_1/2$, by an acousto-optic modulator. A lock-in amplifier synchronized with the modulation frequency is used to extract the signal from a photodiode. This lock-in detection makes it possible to shift the data acquisition at frequency f_2 where laser noise and technical noises are generally low. Such an arrangement allows for the measurement in the time domain of changes in the sample reflectivity in the range $[10^{-4}\text{-}10^{-7}]$ with an upper bandwidth boundary limited by pulse duration. Despite these outstanding capabilities this system has the following limitations: it gives access to the real part of the complex reflection coefficient only; because the mechanical delay line is used, acquisition of a single signal takes a long time, thus preventing the production of images by scanning the sample, especially for living matter; frequency resolution is limited by the repetition frequency f_1; in-plane space resolution is limited by optical diffraction. These limitations have remarkably been overcome thanks to the striking advances mentioned in the following.

4.1. Interferometry

Several techniques were developed early to measure the phase of the reflection coefficient changes, Eq. 13. This provides an interesting alternative for detecting hypersound in materials with small piezo-optic coefficients, as is the case for example for copper at the standard probe wavelength of 780 nm. Overall, it gives access to the acoustic surface displacement, and is thus of notable interest for the study of surface and interface waves in the low GHz range.

Femtosecond interferometry was initially developed to resolve the laser-induced modification of the complex refractive index of a sample, [90] and later applied to picosecond ultrasonics [91,92]. Double path interferometers were the first to be used in the field, notably the Mach-Zehnder [91] and Michelson interferometers [93] where the position of a reference mirror is controlled with an active feed-back loop. Common-path interferometers of the Sagnac type were later in widespread use [92,94,95]. Depending on the temporal delay between the reference and probe pulses at the sample, either the surface displacement or its derivative is measured. Recently an alternative approach was proposed where the beam splitter used in a Sagnac interferometer to create the reference and probe beams was replaced by a birefringent crystal which generates a pair of phase-locked pulses with orthogonal polarizations [96]. The temporal delay between the reference and probe pulse is then imposed by the birefringence of the crystal and by its thickness. When used in reflection mode this single path interferometer with a single birefringent crystal is extremely stable, easy to align and does not need stabilization [97,98].

The use of an optical Fabry-Pérot to enhance the signal detected in picosecond ultrasonic experiments was also investigated. In this method a reflector is placed above the sample surface so that an air optical cavity is formed between the reflector and the sample. Accurate spacing close to the optical resonance is required to access a signal amplification by two orders of magnitude [99].

4.2. Ultrafast signal acquisition

The original experimental method relies on optical sampling with a conventional femtosecond pump-probe setup, where the pump and probe pulses are delivered by the same laser and the probe pulse is time

delayed with respect to the pump pulse by using moving mirrors mounted on a motorized translation stage. This mechanical motion shows several intrinsic drawbacks, such as fluctuation of the beam pointing, modification of the size of the focal spot on the sample and long acquisition times for pump-probe delays ranging over several nanoseconds.

To circumvent these drawbacks, the asynchronous optical sampling technique (ASOPS) was adopted for picosecond ultrasonic experiments [100]. In this alternative scheme, two different optical combs are used for pump and probe pulses. A slight difference Δf_1 between their pulse repetition rates f_1 creates the pump-probe delay, thus the mechanical delay line is no longer needed. Pump-probe delays from zero to the inverse of the repetition rate, $1/f_1$, are scanned during one beating period between pump and probe asynchronous pulse trains, $1/\Delta f_1$, typically in the millisecond range [101]. Such a technique where the sampling is performed at a distinct rate with respect to the excitation is also called equivalent time sampling. Stroboscopic stretching enables the transfer of optical time scales, femtosecond to nanosecond, to electronic time scales, which makes the signal directly recordable by an oscilloscope. Thanks to such ultrafast sampling, low reflectivity changes can be detected by averaging over very large number of time-scans, thus dispensing with the use of lock-in amplification.

ASOPS systems with repetition rates in the GHz range are ideally suited for investigating the propagation of coherent acoustic phonons with frequencies ranging from a few tens of GHz [102] to several THz [103]. The drawback of such ASOPS setups with high repetition rates is that they do not offer a sufficient frequency resolution to investigate the propagation of coherent acoustic phonons in the low- or sub-GHz frequency range. For such investigations, lower repetition rates, typically of $f_1 \approx 50$ MHz [57] or $f_1 \approx 80$ MHz [101,104], offer convenient frequency resolution of that order. In these two-laser systems the slight difference in their repetition rates is actively stabilized with a feedback loop. The temporal resolution of the setup is limited by the jitter between both laser pulse trains, possibly up to several hundred fs.

Recently, a system was demonstrated where a single laser cavity was used to produce two pulse trains with a repetition rate difference [78,105]. A birefringent crystal is inserted in the laser cavity so that the modes with orthogonal polarizations are delayed independently. The system is free-running, since no piezo-electric and electronic stabilization systems are required to control Δf_1. The latter is dependent on the difference in wave speed and on the length of the optical path in the crystal and is intrinsically stable, thus decreasing laser jitter. These advances, introduction of the equivalent time sampling and free running dual comb laser, have not only drastically reduced signal acquisition time, but they have also significantly reduced the complexity and cost of the systems.

4.3. Frequency control

Through opto-acoustic transduction in the absorbing material a single acoustic pulse is periodically generated in the time domain. Owing to its very short monopolar or dipolar nature, this pulse is very broadband in frequency. There are however a myriad of applications where the excitation of acoustic signals with narrower bandwidth around a controlled frequency is desired, although at the cost of a lower time resolution.

Thin film acoustic resonances of the transducer itself can be used for this purpose. Hence, relaxation in amorphous solids was studied with the measurement of phonon attenuation in polymers. For instance, attenuation in PMMA was measured at frequencies up to 320 GHz using thin NiTi films of thickness down to 35 nm as transducer [106]. However, this method lacks versatility because it requires one sample design for each selected central frequency.

Alternatively, optical pulse sequences were produced by inserting a specifically designed pulse-shaper along the pump path. This optical system included partly reflecting mirrors mounted on a translation stage. The period of the sequence can be tuned continuously thus concentrating the acoustic energy at the controlled reciprocal frequency [107]. Narrow band acoustic attenuation measurements could then be achieved in vitreous silica at frequencies ranging from 20 GHz to 400 GHz [108].

With the same aim, the length of the laser cavity can be finely tuned so that the laser repetition frequency f_1 matches the frequency of the desired acoustic excitation. Thus acoustic modes of a free-standing semiconductor membrane were measured with high laser repetition frequencies in the range [0.8–1] GHz [109].

Besides the abovementioned achievements to adequately control the central frequency of a narrow band acoustic generation, attention has been paid to improving the intrinsic frequency resolution. In standard experimental set-ups, the frequency spectrum of the signal comes out multiplied by a frequency comb with a periodicity f_1, reciprocal to the pulse period. Therefore, the best frequency resolution one can expect is limited and is equal to f_1. This can be insufficient for several applications, such as the accurate measurement of the Brillouin frequency in transparent media, acoustic resonances with high Q, or the dispersion curves for surface and interface waves. This can be circumvented by varying the laser repetition rate [109] but for low repetition rates, 50–80 MHz, this implies significant changes in length for the laser cavity, which is difficult to implement in practice.

Another solution was demonstrated by taking advantage of lock-in detection at a modulation frequency f_2 [110]. This is inherently present in the set-ups that use delay lines for optical sampling and can also be introduced in systems using ASOPS. The abovementioned frequency limitation can be overcome by taking advantage of the sidebands at frequencies $f_1 \pm f_2$, and of the complex signal provided by the lock-in detection. Modifying the modulation frequency f_2 thus allows arbitrary acoustic frequency control.

4.4. Space resolution

If a probing technique were demonstrated that would read out the motion of the sample surface, combining nanoscale spatial resolution and picosecond temporal resolution, this would offer outstanding perspectives for nanoscale mechanical characterization. In addition to the techniques mentioned above in Section 2.6 to overcome the optical diffraction limit, using a fiber tip in a SNOM [62,63] or piezoelectric saturation [65], several remarkable achievements have allowed the detection of sound waves with a better lateral resolution than optics. In the following we mention few of them.

A noticeable step towards this goal was achieved with near-field microscopy using a plasmonic nanofocusing probe. In this technique the probe laser is converted into a surface plasmon at the surface of an AFM probe, by etching a diffraction grating on the surface of the probe to couple the incident light and the surface plasmon. The evanescent light was concentrated at the nanoscale apex of the probe and produced a bright local optical source. The optical detection of broadband ultrasound with a frequency of up to 135 MHz was achieved with a similar spatial resolution to the AFM probe tip radius [111].

The excitation of bulk and surface acoustic waves following light absorption by 1D and 2D arrays of metal nanoparticles, and by a single metal nanoparticle, has been highlighted in Section 2.7. Conversely, the optical detection of vibrational modes of 2D and 1D arrays has also been used to detect optically generated surface acoustic waves. Opto-mechanical coupling of the mechanical vibrations of Au nanoparticles and their optical response, due to collective electronic oscillations, has led to the detection of surface acoustic waves by such metallic nano-antenna. The reflectivity changes induced by this plasmonic response have made it possible to detect surface acoustic waves at frequency ≈ 10 GHz propagating along the surface of a glass substrate using lines made of Au and of width ≈ 65 nm [50].

Another mean of detecting surface acoustic waves consists in measuring changes in the optical diffraction of light by an array of

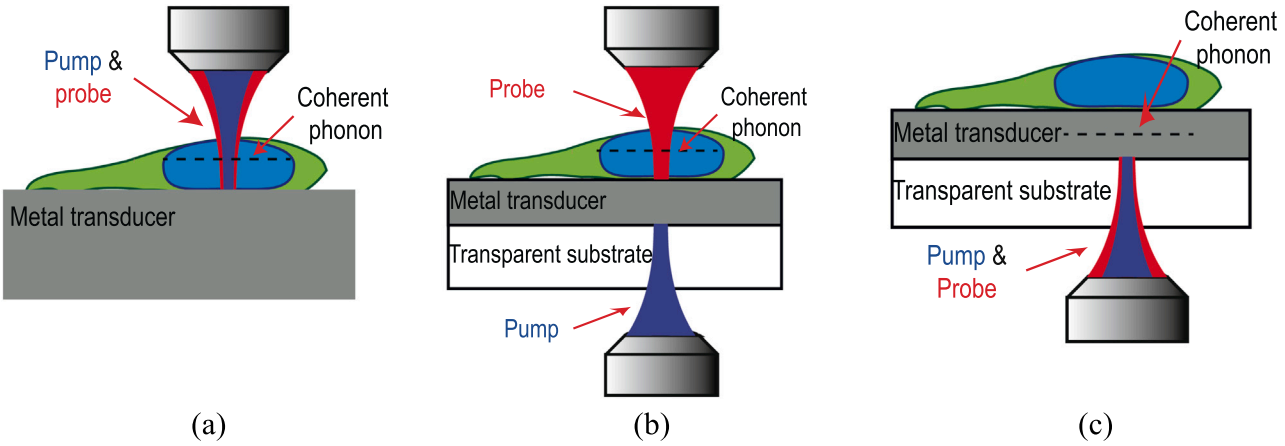

Fig. 5. Pump and probe positions with respect to the sample. (a) Both pump and probe are focused on top of a bulk metal transducer through the cell. TDBS signal is detected in cell. (b) Pump and probe are focused on each side of a thin metal transducer. TDBS signal is detected in cell and acoustic echoes propagating back and forth in the thin metal layer can also be detected because of reflectivity changes at the metal-cell interface. (c) Both pump and probe are focused at the bottom of a thin metal transducer. Acoustic echoes propagating back and forth in the thin metal layer are detected because of reflectivity changes at the substrate-metal interface.

reflectors spread on the material surface, with a period of the array matching the acoustic wavelength in play. The optical diffraction of extreme ultraviolet light (EUV), of wavelength ≈ 30 nm, has permitted the detection of surface acoustic waves at a frequency of ≈ 80 GHz. For this the EUV beam was focused on a 2D array of period 45 nm made of Co/Pd nano-pillars on a Si substrate [112]. Measurement of the velocity of surface acoustic waves of such small wavelength with the diffraction of an EUV beam was used to assess the elastic moduli of ultrathin films with thicknesses down to 11 nm [113].

Besides this 1–2D geometries, acoustic communication between two single Au particles, one used for opto-acoustic generation, the other for detection was also achieved recently in the same frequency range [114]. The modulation of localized surface plasmon resonances of the single receptor, of either the rod or disk shape, was detected in these experiments. These achievements with single nanotransducers are opening up perspectives for the nondestructive evaluation at the nanoscale, notably for soft and biological matter, bearing in mind that such Au nanoparticles could be optically printed at the sample surface [115].

Going further in the acousto-optic space resolution may demand implementing other mechanisms than optical interferometry or plasmonic resonance disturbances. Exploiting the detection of changes in molecule fluorescence due to acoustic disturbances in the molecular surrounding is a direction that was recently suggested [116].

5. Applications to the nanoscale investigation of cell mechanics

Fluorescence microscopy is the current gold standard cell imaging modality as it provides real-time and spatially resolved information on biological structures and internal pathways. Multiple fluorescent dyes can be used with specific proteins and antibodies to highlight structures within the cell. Conversely, opto-acoustic microscopy does not involve the addition of exogenous labels or other contrast agents since it can provide cell imaging with the endogenous mechanical characteristics as the contrast mechanism. Thanks to its outstanding time or frequency resolution, it allows for the quantitative evaluation of the mechanical properties with sub-optical axial resolution.

Cell mechanics is involved in several fundamental biological processes such as adhesion maturation, migration, differentiation and malignant transformation. In addition, as it is intimately related to the fibrous and supra-molecular structures of cell organelles cell mechanics reveals the structural changes continuously occurring during cell cycles. The research effort for studying the mechanics of single cells and subcellular components has thus been growing rapidly with significant results and vast implications for biotechnology and human health. However, current experimental techniques are facing two fundamental limitations: living cells react to the active means used to take measurements, changing their mechanical behavior; and resolving the biomechanical interplay between cell organelles requires their mechanical properties be evaluated independently.

Picosecond opto-acoustics, as a remote label-free modality, shows excellent capacity for the quantitative evaluation and imaging of the intra-cell mechanical properties, currently with a micron in-plane and a sub-optical in-depth resolution. Although most experiments to date have been achieved with fixed cells in air or in liquids, the capacity to image live cells has been demonstrated. In the following we first describe the material and methods used for time domain Brillouin spectroscopy (TDBS) in cells, on one hand, and for cell ultrasonography on the other. Then the applications of these opto-acoustic imaging modalities to address biologic questions are presented. However, the future challenges for further developments in applications of the technique to biology will not be developed extensively here.

5.1. Time domain Brillouin microscopy in cell organelles

The absorption of fs pump pulses over the nanometric skin depth of the biocompatible metal transducer on which the cell was grown, Fig. 5, launches an acoustic wavefront in cell. Its propagation along the cell thickness is detected with probe light in cell through the Brillouin acousto-optic interaction, Section 3.2 [15]. The pump beam can be focused at the cell-metal interface, Fig. 5(a), then a bulk transducer can be used, or at the bottom interface of a thin metal layer sputtered on a transparent supporting substrate, Fig. 5(b). In the latter case, the hypersound is partially reflected and partially transmitted to the cell owing to the acoustic impedance mismatch. Titanium was used as a bio-compatible metal, and sapphire [117] or silicon [118] as a supporting transparent medium as their high thermal diffusivity minimizes heat accumulation at the metal-cell interface. Two distinct improvements have been brought to the design of the thin metal transducer. A composite transducer was made of thin alternating layers of two materials, one with a high optical absorption, the other with a high thermal conductivity and thermal expansion coefficient. Optically induced heating of the thin layer diffuses into neighboring layers and, within a time less than $1/f_B$, produces their large expansion resulting in the enhanced generation of coherent acoustic waves [119]. Using another approach, where both pump and probe lasers were focused at the bottom of the structure, Fig. 5(c), a three-layered transducer was designed to produce an optical cavity where the pump is absorbed and the probe is transmitted through. This enables the TDBS signal to be detected with

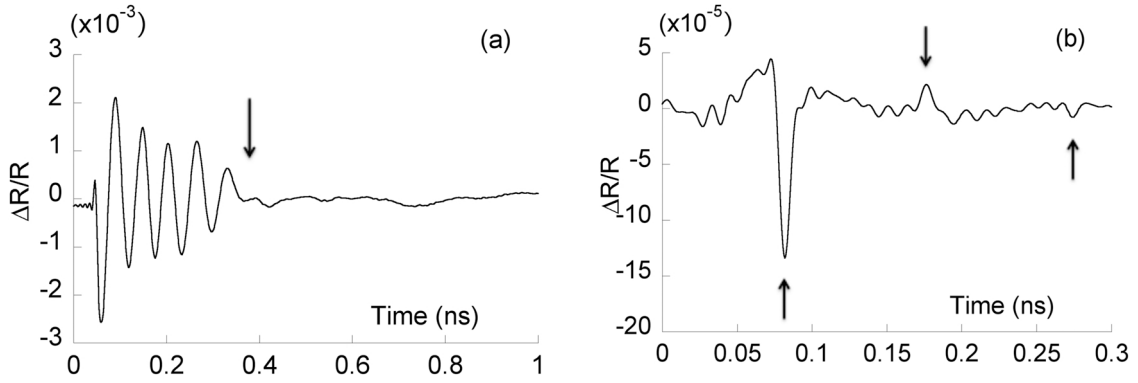

Fig. 6. Relative changes in reflectivity measured with a fixed macrophage cell on a 300 nm thick titanium film on a sapphire substrate. The pump beam was focused at the sapphire-titanium interface. In (a) the probe is focused at the cell-titanium interface. The time domain Brillouin scattering reveals propagation in cell of phonons at frequency $f_B \approx 16.5$ GHz. The arrow shows time when the phonons reach the cell surface. In (b) the probe was at the transparent substrate - metal film interface. Arrows point out echoes bouncing back and forth through the metal film.

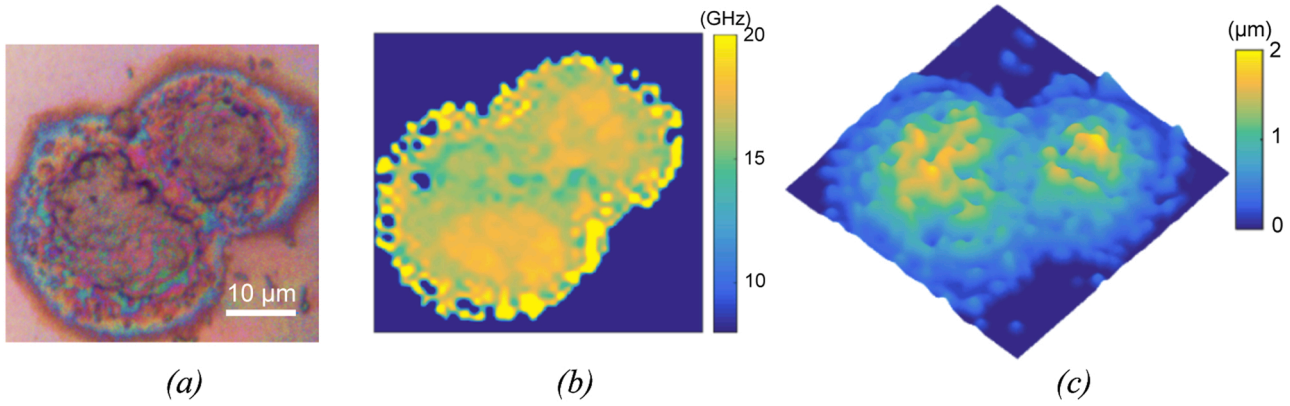

Fig. 7. (a) Top view image of a macrophage under white light illumination. The cell shows a typical early telophase or late anaphase nuclear morphology of bi-lobed structure, a single nucleus dividing into two daughter cells of approximately 15 μm in diameter. (b) Map of Brillouin frequency. (c) 3D map of cell thickness. Adapted from J. Biophotonics. 2019; e201900045 with permission of John Wiley and Sons.

minimum laser intensity in cell [120].

The recorded signals allow for measurement of the frequency f_B of the time-resolved Brillouin oscillations and of their lifetime τ. This frequency is typically in range [5–20] GHz depending on probe wavelength and cell hydration. Given the refractive index in cell, the sound velocity at the Brillouin frequency can be calculated, as mentioned in Section 3.2. From the general equation governing acoustic propagation in a viscoelastic medium, the complex modulus M can be expressed by:

$$M = M' + jM'' = \rho V^2 + j\frac{\rho V^2}{\pi f_B \tau} \tag{23}$$

with the real and imaginary parts describing the longitudinal storage and loss moduli, respectively. TDBS measurements can therefore be used to assess the complex modulus, given the known mass density, ρ, and optical refractive index, n, of the sample [121]. Note, however, that the loss tangent, $tan\delta = M''/M'$, that characterizes acoustic dissipation in cell, does not depend on ρ nor on n.

For the purpose of illustration the signal detected with the probe focused at the film-cell interface, Fig. 5(b), is shown in Fig. 6(a) for a macrophage cell, on a 300 nm thick titanium film on sapphire. The cell is fixed, dehydrated and experiments are performed in air. Large Brillouin oscillations reveal propagation of coherent phonons at $f_B \approx 16.5$ GHz in the cell nucleus.

The presence of a stepwise signature in the measured waveform, as labeled with an arrow in Fig. 6(a), marks the moment when the coherent acoustic phonons reach the top surface of the cell nucleus. With the predetermined sound velocity, one can thus simultaneously obtain the nucleus thickness. This measurement however requires that the cell thickness be less than the phonon propagation distance, typically in range [3–5] μm at frequencies in play. For the thinner parts of the cell, typically the cytoplasm surrounding the nucleus, thicknesses can be assessed measuring the acoustic resonance frequencies of the thin cell layer. This 3D mapping of cell morphology has been compared with measurement performed by AFM on a same fixed macrophage cell in air [122].

Fig. 7 shows the Brillouin frequency map and thickness map of a macrophage cell. The nuclear morphology, Fig. 7(a), indicates that the cell is mitotic, typically in early telophase or late anaphase. The Brillouin map, Fig. 7(b) shows with high contrast the mechanical landscape of the nuclei. The image unravels two distinct regions near the pole of each daughter nucleus that cannot be observed from the optical image in Fig. 7(a): an orange part with Brillouin frequencies around 18 GHz enclosed by a green part with lower Brillouin frequencies around 15 GHz, measured with a probe wavelength at 515 nm. This inhomogeneity possibly arises from the chromosome segregation and remodeling occurring in the late anaphase, in which chromosomes are drawn to opposite poles of the nucleus and reach their maximum condensation to help chromosome segregation and the re-formation of the nucleus in the telophase. Fig. 7(c) shows the 3D cell morphology measured with the acoustic data. The thickness map suggests that cell thickness is maximum, approximately 2 μm, around the center of each daughter nucleus rather than at the pole side, where the Brillouin frequency is at its maximum. This comparison is worthy of note since it

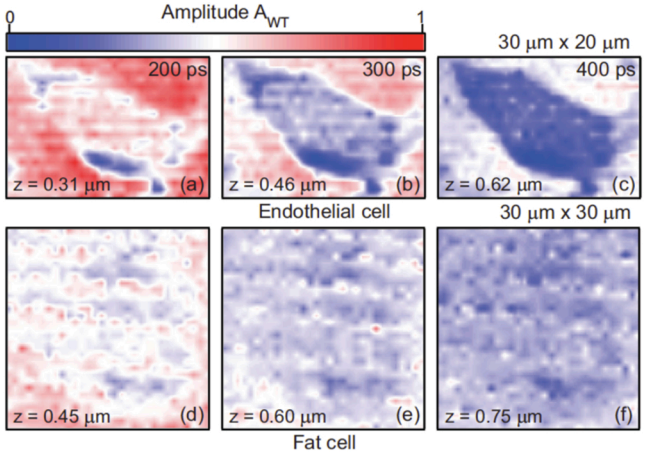

Fig. 8. Signal amplitude at the Brillouin frequency in bovine endothelial (a-c) and mouse adipose (d-f) cells at increasing distances from the metal transducer. Reproduced from Appl. Phys. Lett. 106(16) (2015) 163701 with the permission of AIP Publishing.

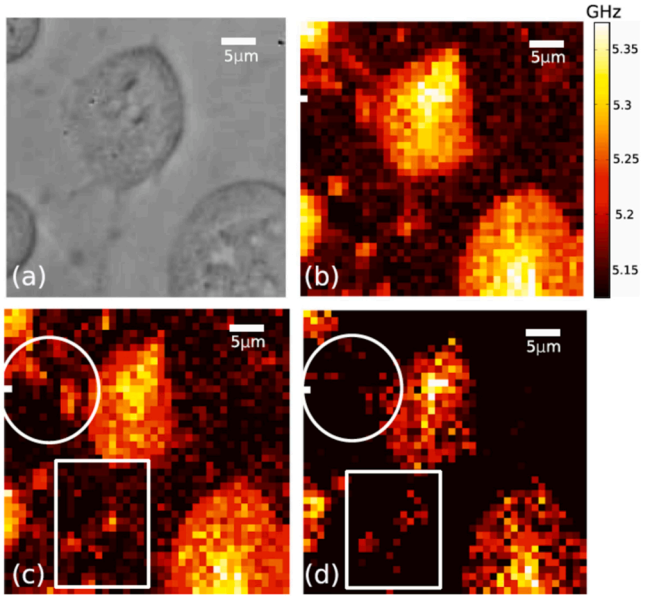

Fig. 9. (a) Optical image of the live 3T3 cells. (b) Map of the Brillouin frequency shift with probe wavelength at 780 nm. Sections at distance of (c) 1 µm and (d) 1.8 µm from the transducer. Thin filopodia (marked by white circle, square) are resolved axially as the section moves deeper into the cell. Reproduced from Scient. Reports 6 (2016) 39326.

suggests the Brillouin frequency, a gauge for chromatin condensation, is independent of the cell thickness [123].

Because the Brillouin oscillations are time-resolved, changes in either the signal amplitude or the Brillouin frequency shift with time, i.e. with coherent acoustic phonon propagation in depth, can be measured. For this, the phonon velocity measured with the Brillouin frequency shift is used to convert the sub-picosecond time scale into a sub-micrometer scale in depth, z. The in-depth resolution is then limited by the acoustic wavelength $\lambda/2n$, with n the refractive index for cell, see Section 3.2. This depth profiling of the signal amplitude at the Brillouin frequency-shift was achieved with bovine endothelial, mouse adipose[124] and mouse 3T3[125] fixed cells in buffer solution. Fig. 8 shows amplitude of the signal at the Brillouin frequency for endothelial and fat cell. In this figure slices of the signal amplitude are at a distance of $\lambda/2n \approx 150$ nm. The ultrasonic attenuation in the endothelial cell is clearly greater than

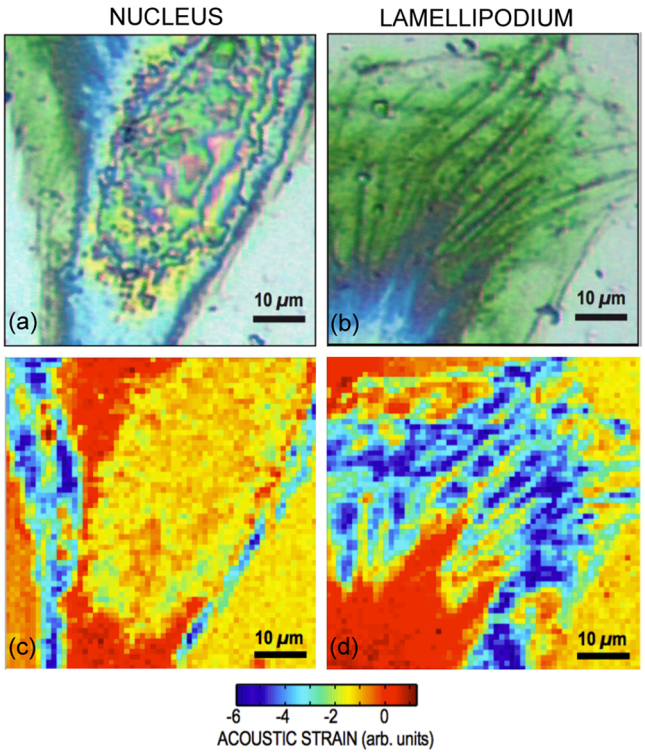

Fig. 10. (a) Images of the nuclear region (a) and lamellipodium (b) of a human mesenchymal stem cell migrating upward. The first row shows top view white-light images for comparison. Raw acoustic images of the amplitude of the first echo reflected at the transducer-cell interface in the nuclear region (c) and in the lamellipodium (d). Adapted from Scient. Reports 5 (2015) 1038.

that of its surroundings, whereas attenuation in the fat cell is similar. The spatial dependence shows evidence of inhomogeneity of the acoustic dissipation inside the cells [124].

The depth profiling of the Brillouin frequency-shift, shown in Fig. 9, was demonstrated with live 3T3 mouse fibroblasts[126]. The contrast as shown in the Fig. 9(c-d) was obtained by calculating the Brillouin frequency along a time window of six acoustic cycles giving a slice thickness of 840 nm. The cell morphology and extent are shown to change as the section is shifted through the cell. For instance, the filipodial structures, highlighted with circle and square in Fig. 9(c-d), are shown to be thinner as the distance increases [126].

5.2. *Single cell ultrasonography*

Alternatively, a pulsed opto-acoustic microscope was demonstrated, where both the pump and probe beams are focused at the bottom of a metal monolayer transducer, Fig. 5(c). In this situation the transparent medium that supports the film acts as a heat sink, and the layer thickness is designed to ensure that the cell remains thermally isolated [117]. This inverted microscopy leaves the cell undisturbed from laser radiation and laser heating. This architecture of the opto-acoustic modality leaves room for simultaneous fluorescent microscopy of the cell from top.

The focusing of low-energy femtosecond pump laser pulses at the bottom of the metal film produces an ultrafast thermal expansion and launches a longitudinal acoustic pulse in the metal film, with a broad spectrum extending up to 100 GHz. The transient changes in the probe optical reflectance allow measurement of the amplitudes of echoes bouncing back and forth through the film, as shown in Fig. 6(b). Fig. 10 shows images of a fixed human mesenchymal stem cell, hMSC on a thin titanium layer [127]. The cell is highly polarized as it undergoes migration, and the nucleus region and the lamellipodium were selected for the acoustic imaging. The top-view white-light image, Fig. 10(a),

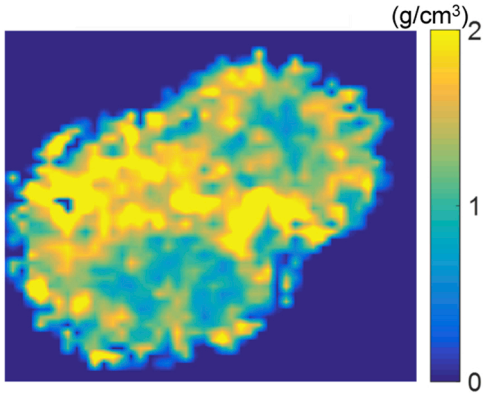

Fig. 11. Map of the mass density (g/cm^3) measured in the nucleus of the mitotic macrophage shown in Fig. 7. Adapted from J. Biophotonics. 2019; e201900045. with permission of John Wiley and Sons.

suggests that the cell height is at a maximum in the nuclear region and decreases dramatically in the peripheral ruffles. Bundles of actin filaments appear as darker stripes perpendicular to the cell edges in Fig. 10 (b). This contractile structure is continuously remodeled to allow displacement of the cell in treadmill-like motion. Fig. 10(c, d) are maps of the amplitude of the acoustic echoes reflected at the transducer-cell interface. The very high acoustic contrast reveals the cell morphology and that of the cell components. The thin cytoplasm at the cell periphery and the structure of the nucleus are clearly shown in Fig. 10(c). The actin network and the fine details of the leading edge of the lamellipodium are distinctly resolved in Fig. 10(d) [127].

The reflection of acoustic waves at the interface between the titanium film and an acoustically thick cell is dominated by the mismatch in acoustic impedances. The contrast in the acoustic images in Fig. 10 is related to spatial variations in the cell impedance Z_c, caused by rigidity and mass density fluctuations within the cell. However, acoustic contrast that depends on frequency indicates that other mechanisms, inherent to ultrasonography at a nanoscale, need to be accounted for. In analogy to conventional pulse echo experiments,[128] changes in the acoustic reflection coefficient with frequency can be attributed to cell adhesion. The balance between the adhesive and repulsive forces maintains the cell at equilibrium. The high-frequency acoustic nano-pulses impinging on the surface disrupt this equilibrium. This spring-like interface gives a frequency dependence of the acoustic reflectance. Therefore by processing the changes with frequency, in range [10–100] GHz, film-cell interfacial stiffness K can be measured [129].

Variations in Z_c across the cell are attributed to rigidity and density fluctuations within the cell, whereas variations in K are related to interfacial intermolecular forces and to the nano-architecture of the trans-membrane bonds [129]. Notably, maps with a micron in-plane resolution of the impedance and interfacial stiffness were produced in cell nuclei and in the lamellipodium of a migrating hMSC [127].

Dual-probe architecture was demonstrated where the probe beam is split into two to build two arms for probing the sample from the bottom and top simultaneously [123,130]. This combines the set-ups shown in Fig. 5(b) and Fig. 5(c) into a single one, with one pump beam and two opposite probe arms aligned along the same axis. As the acoustic pulses are partly reflected at the metal-cell interface, cell ultrasonography is achieved with the bottom probe arm; and as they are partly transmitted to the cell, the TDBS imaging of the cell is made possible simultaneously with the top probe arm. For each individual pixel in the image, opto-acoustic signals are acquired from each channel in a single run measurement at a single spatial location. Therefore the physical data of experimental access are cell impedance and adhesion stiffness, with the bottom probe arm, and cell thickness and hypersound velocity and attenuation, calculated with the time-domain Brillouin signals, measured with the top probe arm. According to the current state of the art a uniform refractive index is the only unique input. However, the contrast in the opto-acoustic images [123] is still greater than the inhomogeneity of the refractive index one may expect for a biological cell [131]. With these data in hand, notably the acoustic impedance, acoustic velocity and dissipation, one can merely extrapolate and map the complex stiffness modulus and the mass density in cell with an optical resolution. This is a noticeable step forward given that maps of these latter physical parameters are easier to interpret biophysically than hypersound velocity or acoustic impedance. For instance, we show in Fig. 11 the map of mass density we measured with the dual probe architecture in the nucleus of the mitotic macrophage shown in Fig. 7. It reveals two distinct regions in opposite correlation with maps of the Brillouin frequency Fig. 7(b). This suggests that the mass density of dense chromosome network at poles is less than mass density of the nucleoplasm [123].

5.3. Contributions for biomechanics

In this section we shine a light on the inputs that opto-acoustic microscopy can provide to help investigations in biomechanics and connections with biology. The strengths and weaknesses of the technique with respect to state of the art alternative methodologies are not developed but they can be found in the literature we refer to in this section. Unless explicitly mentioned, the above reported results have been achieved with fixed cells.

Cell 3D morphology, nucleus roughness. Cell morphological analysis has long been used in cell biology and physiology for abnormality identification, early cancer detection, and dynamic change analysis under specific environmental stresses. In such investigations, cell biologists usually use cell images provided by optical microscopy. Although this approach delivers detailed information about cells' inner/outer structures, it offers only planar two-dimensional information. A few interferometric imaging techniques provide access to the in-depth information. However, the axial resolution is limited, generally ranging from a few microns to sub-microns. In addition, dispersion in cell thickness, i.e. nano-scale cell roughness, is an interesting indicator of the cell's state of health. It can be altered by a modification of the membrane ultrastructure, [132] or by a disorganization of the nucleus microstructure, as observed for cancer cells [133].

Picosecond opto-acoustic microscopy shows unique capabilities to provide cell 3D morphologies. Thicknesses in the range [10–50] nm were mapped in between microtubules in the thin leading edge of a migrating hMSC, thus solving microtubules and showing typical cell morphological structures of migrating cells such as arches [127]. TDBS was also applied to provide the entire 3D morphology of an osteosarcoma cell, the roughness of which is known as biologically relevant. It was also obtained using AFM as a reference mean for contact thickness measurement. The good agreements of the measured profiles and mean thicknesses confirmed accuracy of the remote technique for measuring cell thicknesses as small as $\lambda/7$. In addition, the in-plane definition of ≈ 1 μm, as limited by optical diffraction, was shown to be convenient for performing relevant roughness analysis. A sensitivity to nucleus roughness of the order of $\lambda/10$ was demonstrated. This is a remarkable input since nucleus roughness is an important morphological phenotype for cancer cells [134].

Cell adhesion. Cell adhesion plays an integral role in several biological processes such as migration, mechanosensing, morphogenesis or differentiation [135,136]. When placed on a surface, a cell attaches to discrete specialized areas called focal adhesions, [137] where the cell anchors to the surface by providing mechanical bondings, formed by nanoscale clustering of a tremendous number of trans-membrane proteins [138]. The cell-substrate mechanics are thus highly heterogeneous and unraveling the mechanics of cell adhesion requires sub-cell characterization. Research in these fields requires techniques to characterize cell adhesion in order to better understand, control and optimize it with

various types of substrate.

Picosecond acoustic ultrasonography has shown its capability to measure the cell-surface adhesion stiffness, currently with an in-plane resolution limited by the optical diffraction limit. The uniform adhesion of monocytes was first measured [129] and the adhesion stiffness microscopy later unraveled strong isolated adhesion sites scattered at the surface underneath the nucleus of mitotic macrophage-like cells [123]. Advances in the technique have since made it possible to acquire a larger number of pixels for each cell and to perform this set of acquisitions for a large number of cells from the same sample [139]. The resulting finding has demonstrated a tendency in endothelial cells to develop a larger number of sites of strong adhesion when cells are in contact with each other than when isolated on the transducer surface, as if a cell was developing trans-membrane adhesion proteins when sensing the presence of another cell. This shows that picosecond acoustic ultrasonography can reveal active processes involved in cell adhesion and can dissociate them from passive processes [140]. Moreover, this active adhesion was shown to be correlated with changes in the elastic homogeneity of the nucleus.

Nucleus compressibility and elastic homogeneity. The interior of the nucleus has a complex composition that consists mainly of DNA molecules packed in compacted histone-DNA complexes to form chromatin fibers. Through epigenetic regulation, chromatin can be packaged into different conformations and compactions that modulate gene expression and access of transcription factors to their binding sites [141,142].

Chromatin fiber has been identified as the major load-bearing element of the nucleus, [142] and the chromatin condensation state dictates the nuclear stiffness [143]. It forms supra-molecular condensates in the nucleus in which chromatin is physically constrained and solid-like, thus forming a solid scaffold [144]. As the phonon wavelength in TDBS experiments, $\lambda/2n$, is longer than the characteristic fiber and interstice diameters homogenization theory applies to describe the mechanical behavior probed by TDBS. In this context, the measured effective storage modulus, Eq. 23, depends primarily on chromatin compaction and conformation [145] and the loss modulus reveals dissipation due to fiber flexibility or to scattering by in-homogeneities of a size close to the phonon wavelength.

In the following we give examples where the cell response induces changes in chromatin organization and we mention the achievements regarding the probing of these changes with the picosecond ultrasonics technique.

Many studies on stem cell differentiation have shown that mechanical cues, both external like shear stress and substrate stiffness, [146] and internal such as the cell's cytoskeleton tension, [147] influence the commitment of stem cells to certain lineage. Strain transfer to the nucleus and subsequent deformation of the nucleus have been proposed as a direct link between mechanical inputs from the microenvironment and gene regulation [148]. This link is mediated by the cytoskeleton forming a mechanically continuous network within the cell allowing the transmission of extracellular mechanical signals to the nucleus. This network favors transfer of mechanical signals to the chromatin. The influence of a pre-tensed cytoskeleton on chromatin compaction and gene expression has been illustrated [148,149]. These studies show that changes in cytoskeleton organization impact on how cell sense and respond to mechanical signals.

The interplay of internal nuclear nanostructure with the intracellular micro-environment was probed with TDBS measurements in cells treated with nocodazole, a chemical agent known to disrupt microtubules [150]. The expected increase in the Brillouin frequency confirmed that the intra-nuclear mechanics can be affected by the cytoskeletal behavior [151].

Another illustration of the probing of cell mechano-transduction with picosecond ultrasonics was found from statistics of measurements obtained from human microvascular endothelial cells cultured for two different times on the metal transducer before fixation. It was shown from acoustic data that the larger number of adhesion sites underneath the nucleus was correlated with the dispersion of nucleus impedance data, with the latter revealing the mechanical inhomogeneities arising from the multiplicity of local conformations within the nucleus [140]. These experiments illustrated the relevance of the combined study of cell adhesion and elasticity, as provided by picosecond ultrasonography.

By using the dual probe architecture mentioned above maps of the acoustic impedance and of the mass density of macrophage cells in the mitosis phase were produced. The nucleus had the characteristics of a telophase with the chromatin, which seems of low mass density, being grouped at two poles while the microtubules and the actin filaments, of greater mass density, work to split the nucleus, Fig. 11 [123].

Gene integrity is continuously challenged by DNA lesion, caused by normal metabolic activities or by environmental factors. In the event of a DNA break, the cell activates DNA damage response pathways that allow detection and repair of the lesion. Failures to repair are important sources of genome instability, giving rise to chromosomal aberrations and severe biological consequences including tumorigenesis and cell death [152,153]. However, DNA damage and repair lead to the activation of different biochemical pathways and to nuclear chromatin reorganization [154,155].

The possibility of measuring the storage and loss moduli inside a cell nucleus is an advance offered recently by PU microscopy. It gives access to the nucleus nanostructure and compaction and rigidity of chromatin fibers, composed mainly of histones and DNA [156]. After DNA damage was induced in osteosarcoma nuclei by either chemical or physical means, the measurement of the complex moduli of the nucleus interior was achieved. After double strand breaks have been induced, the drop in measured stiffness and dissipation revealed the decompaction of the chromatin network, facilitating the access of signaling and repair proteins.

Opto-acoustic microscopy of cell is a newly developed method to explore the cell mechanics, and recent achievements have raised the technique to a high level of maturity. Future developments concern, on the one hand experimental devices whose simplicity has been increasing and whose cost can be expected to decrease still. On the other hand, as with any laser microscopy technique, efforts are continuously maintained to reduce the exposure time to lasers. Although the doses absorbed by the cell are lower than for many other optical modalities, avenues for progress can be found by developing devices that can improve the compromise between the search for efficient opto-acoustic transduction and minimum heat-induced cell stress. Moreover, a large number of applications, particularly in diagnostics, concern measurements with fixed cells and require high data acquisition speed and data throughput. The development of new imaging strategies, for example using multi-channel acquisition systems, is one way that could be considered.

6. Conclusion

The basic physics involved in picosecond ultrasonics has been presented in this paper. By using short laser pulses in highly absorbing materials one can master coherent acoustic pulses with unequaled frequency bandwidth. In a pump-probe experimental arrangement their remote detection is achieved by measuring the perturbation of short light pulses by the acoustic transients. The advances in this field have raised the technique to a high level of development that has been partly described in this article.

With the development of suitable methods and devices it is now possible to demonstrate the ability of this technique to image the properties of individual cells. Image resolution can be better than standard optics and contrast comes from the endogenous mechanical properties of the cell. Another major feature of opto-acoustic microscopy is that it can probe the internal mechanical properties of organelles. The strong sensitivity of the technique to changes in mechanical properties measured inside the nucleus makes it possible to probe changes in the compaction of chromatin fibers, their flexibility or the formation of

Table 1
Physical data used for simulations. Values for piezo-optic coefficients are estimates from fittings of experimental results with calculated signals.

	Sapphire	Titanium	Silica	Tungsten
n (@515 nm)	1.75	$1.78 + 2.05\,j$	1.5	$3.78 + 2.72\,j$
n (@1030 nm)	1.75	$2.95 + 4.10\,j$	1.5	$3.78 + 2.72\,j$
β^{-1} (@515 nm)		20		18.5
β^{-1} (@1030 nm)		20		18.5
$\partial n/\partial \eta$	0.08	$10 + 9\,j$	-0.43	$5.1 + 2.0\,j$
κ (W.m^{-1}. K^{-1})	35	21.9	0.8	174
C_p (J.kg^{-1}. K^{-1})	761	528	700	132
α (10^{-6} K^{-1})	5.8	9	11	4.5
ρ (g.cm^{-3})	3.98	4.5	2.52	19.3
C (GPa)	481.58	220.57	84	308

aggregates. It was possible to measure the supra-molecular changes in these quantities that accompany processes induced by chemical or physical means.

Picosecond opto-acoustic microscopy is thus currently a mature technique, although not yet fully explored, which is providing new vistas on cell mechanics. Its ability to provide complementary insights into cell response to biological cues was demonstrated and it can now be applied to various other fundamental biological cellular processes. From a translational perspective, the mechanical phenotypes that this technique can help identify could be applied to early stage diagnostics of diseases.

Declaration of Competing Interest

The authors declare that they have no known competing financial interests or personal relationships that could have appeared to influence the work reported in this paper.

Data availability

Data will be made available on request.

Acknowledgements

The author acknowledges contributions by L. Le Ridant and Z. Maslah for carrying out the simulations, by L. Liu for upgrading methods and devices and for running the experiments, and by F. Bruno for fruitful discussions on the experiments and calculations.

Appendix

See Table 1.

References

[1] A.A. Oraevsky, S.L. Jacques, F.K. Tittel, Measurement of tissue optical properties by time-resolved detection of laser-induced transient stress, Appl. Opt. 36 (1) (1997) 402–415.
[2] L.V. Wang, S. Hu, Photoacoustic tomography: in vivo imaging from organelles to organs, Science 335 (2012) 1458.
[3] B. Cox, J.G. Laufer, S.R. Arridge, P.C. Beard, Quantitative spectroscopic photoacoustic imaging: a review, J. Biomed. Opt. 17 (6) (2012), 061202.
[4] C. Thomsen, J. Strait, Z. Vardeny, H.J. Maris, J. Tauc, J.J. Hauser, Coherent phonon generation and detection by picosecond light pulses, Phys. Rev. Lett. 53 (1984) 989–992.
[5] H.T. Grahn, H.J. Maris, J. Tauc, Picosecond ultrasonics, IEEE J. Quantum Electron. 25 (1989) 2562.
[6] A. Devos, A. Le Louarn, Strong effect of interband transitions in the picosecond ultrasonics response of metallic thin films, Phys. Rev. B 68 (2003), 045405.
[7] O.B. Wright, T. Hyoguchi, Ultrafast vibration and laser acoustics in thin transparent films, Opt. Lett. 16 (1991) 1529.
[8] G. Tas, J.J. Loomis, H.J. Maris, A.A. Bailes, L.E. Seiberling, Picosecond ultrasonics study of the modification of interfacial bonding by ion implantation, Appl. Phys. Lett. 72 (1998) 2235.
[9] M. Hettich, A. Bruchhausen, S. Riedel, T. Geldhauser, S. Verleger, D. Issenmann, O. Ristow, R. Chauhan, J. Dual, A. Erbe, E. Scheer, R. Leiderer, T. Dekorsy, Modification of vibrational damping times in thin gold films by self-assembled molecular layers, Appl. Phys. Lett. 98 (2011), 261908.
[10] A. Devos, P. Emery, Thin-film adhesion characterization by Colored Picosecond Acoustics, Surf. Coat. Technol. 352 (2018) 406–410.
[11] J.C.D. Faria, P. Garnier, A. Devos, Non-destructive spatial characterization of buried interfaces in multilayer stacks via two color picosecond acoustics, Appl. Phys. Lett. 111 (2017), 243105.
[12] G. Tas, H.J. Maris, Electron diffusion in metals studied by picosecond ultrasonics, Phys. Rev. B 49 (1994) 15046.
[13] H. Maris, Picosecond ultrasonics, Sci. Am. 278 (1) (1998) 86.
[14] L.J. Shelton, F. Yang, W.K. Ford, H.J. Maris, Picosecond ultrasonic measurement of the velocity of phonons in water, Phys. Status Solidi (b) 242 (7) (2005) 1379–1382.
[15] C. Rossignol, N. Chigarev, M. Ducousso, B. Audoin, G. Forget, F. Guillemot, M. C. Durrieu, In vitro picosecond ultrasonics in a single cell, Appl. Phys. Lett.. 93 (2008), 123901.
[16] P. Ruello, V.E. Gusev, Physical mechanisms of coherent acoustic phonons generation by ultrafast laser action, Ultrasonics 56 (2015) 21–35.
[17] V.E. Gusev, O.B. Wright, Ultrafast nonequilibrium dynamics of electrons in metals, Phys. Rev. B 57 (5) (1998) 2878–2888.
[18] Bold letters denote vectors and matrices. The dimension of matrices is indicated with an upper left index.
[19] C. Kittel. Solid State Physics, seventh ed, Wiley, New York, 1995.
[20] S.I. Anisimov, B.L. Kapeliovich, T.L. Perel'man, Electron emission from metal surfaces exposed to ultrashort laser pulses, Sov. Phys. JETP 39 (1975) 375–377.
[21] C.-K. Sun, F. Vallée, L.H. Acioli, E.P. Ippen, J.G. Fujimoto, Femtosecond-tunable measurement of electron thermalization in gold, Phys. Rev. B 50 (20) (1994) 15337–15348.
[22] T. Dehoux, N. Chigarev, C. Rossignol, B. Audoin, Effect of lateral electronic diffusion on acoustic diffraction in picosecond ultrasonics, Phys. Rev. B 77 (2008), 214307.
[23] A. Yamamoto, T. Mishina, Y. Masumoto, M. Nakayama, Coherent oscillation of zone-folded phonon modes in GaAs-AlAs superlattices, Phys. Rev. Lett. 73 (5) (1994) 740–743.
[24] C. Thomsen, H.T. Grahn, H.J. Maris, J. Tauc, Surface generation and detection of phonons by picosecond light pulses, Phys. Rev. B 34 (1986) 4129–4138.
[25] J.F. Young, H.M. Van Driel, Ambipolar diffusion of high-density electrons and holes in Ge, Si, and GaAs: many body effects, Phys. Rev. B 26 (1982) 2147–2158.
[26] O.B. Wright, V.E. Gusev, Acoustic generation in crystalline silicon with femtosecond optical pulses, Appl. Phys. Lett. 66 (1995) 1190–1192.
[27] N.V. Chigarev, D.Yu Paraschuk, X.Y. Pan, V.E. Gusev, Coherent phonon emission in the supersonic expansion of photoexcited electron-hole plasma in Ge, Phys. Rev. B 61 (2000) 15837–15840.
[28] H.W. Lord, Y.A. Schulman, A generalized dynamical theory of thermoelasticity, J. Mech. Phys. Solids 15 (1967) 299–309.
[29] R.G. Stearns, G.S. Kino, Effect of electronic strain on photoacoustic generation in silicon, Appl. Phys. Lett. 47 (1985) 1048–1050.
[30] B. Audoin, H. Meri, C. Rossignol, 2D diffraction of plasma, thermal and elastic waves generated by an IR laser pulse in semiconductors, Phys. Rev. B 74 (2006), 214304.
[31] P. Babilotte, P. Ruello, G. Vaudel, T. Pezeril, D. Mounier, J.-M. Breteau, V. Gusev, Picosecond acoustics in p-doped piezoelectric semiconductors, Appl. Phys. Lett. 97 (2010), 174103.
[32] P. Ruello, T. Pezeril, S. Avanesyan, G. Vaudel, V. Gusev, I.C. Infante, B. Dkhil, Photoexcitation of gigahertz longitudinal and shear acoustic waves in BiFeO3 multiferroic single crystal, Appl. Phys. Lett. 100 (2012), 212906.
[33] H. Tanaka, T. Sonehara, S. Takagi, A new phase-coherent light scattering method: first observation of complex Brillouin spectra, Phys. Rev. Lett. 79 (1997) 881–884.
[34] R.M. Herman, M.A. Gray, Theoretical prediction of the stimulated thermal Rayleigh scattering in liquids, Phys. Rev. Lett. 19 (1967) 824–828.
[35] E. Merino, M. Ribagorda, Control over molecular motion using cis-trans photoisomerization of the azo group, Beilstein J. Org. Chem. 8 (2012) 1071–1090.
[36] O.M. Tanchak, C.J. Barrett, Light-induced reversible volume changes in thin films of Azo polymers: the photomechanical effect, Macromolecules 38 (2005) 10566–10570.
[37] E.S. Pavlenko, M. Sander, S. Mitzscherling, J. Pudell, F. Zamponi, M. Rössle, A. Bojahra, M. Bargheer, Azobenzene-functionalized polyelectrolyte nanolayers as ultrafast optoacoustic transducers, Nanoscale 8 (2016) 13297–13302.
[38] O. Matsuda, O.B. Wright, D.H. Hurley, V.E. Gusev, K. Shimizu, Coherent shear phonon generation and detection with ultrashort optical pulses, Phys. Rev. Lett. 204 (2004), 095501.
[39] T. Pezeril, P. Ruello, S. Gougeon, N. Chigarev, D. Mounier, J.-M. Breteau, P. Picart, V. Gusev, Generation and detection of plane coherent shear picosecond acoustic pulses by lasers: experiment and theory, Phys. Rev. B 75 (2007), 174307.
[40] V. Gusev, P. Picart, D. Mounier, J.-M. Breteau, On the possibility of ultrashort shear acoustic pulse excitation due to the laser-induced electrostrictive effect, Opt. Commun. 204 (2002) 229–236.
[41] M. Lejman, G. Vaudel, I.C. Infante, P. Gemeiner, V.E. Gusev, B. Dkhil, P. Ruello, Giant ultrafast photoinduced shear strain in ferroelectric BiFeO3, Nat. Commun. 5 (2014) 4301.
[42] T. Bienville et B. Perrin, Generation and detection of quasi transverse waves in an anisotropic crystal by picosecond ultrasonics, Proceedings of the WCU 2003, Paris, 2003.

[43] C. Rossignol, J.-M. Rampnoux, M. Perton, B. Audoin, S. Dilhaire, Generation and detection of shear acoustic waves in metal sub-micrometric films with ultra-short laser pulses, Phys. Rev. Lett. 94 (2005), 166106.

[44] S.M. Nikitin, V. Tournat, N. Chigarev, A. Bulou, B. Castagnede, A. Zerr, V. Gusev, Directivity patterns and pulse profiles of ultrasound emitted by laser action on interface between transparent and opaque solids: analytical theory, J. Appl. Phys. 115 (2014), 044902.

[45] B. Audoin, M. Perton, N. Chigarev, C. Rossignol, Diffraction of picosecond bulk longitudinal and shear waves in micron thick films; application to their nondestructive evaluation, Ultrasonics 48 (2008) 574–577.

[46] A. Viel, B. Audoin, Directivity of GHz acoustic waves launched by the absorption of short laser pulses at the interface between a transparent and an absorbing material, J. Appl. Phys. 123 (2018), 043102.

[47] A. Amziane, L. Belliard, F. Decremps, B. Perrin, Ultrafast acoustic resonance spectroscopy of gold nanostructures: towards a generation of tunable transverse waves, Phys. Rev. B 83 (2011), 014102.

[48] N. Chigarev, T. Dehoux, C. Rossignol, B. Audoin, V. Levin, Surface waves in highly ordered poly-graphite and gold micro layers studied by picosecond ultrasonics technique, J. Phys. Conf. Ser. 92 (2007) 012029.

[49] A. Devos, S. Sadtler, P.-A. Mante, A. Le Louarn, P. Emery, Pushing the limits of acoustics at the nanoscale using femtosecond transient interferometry, Appl. Phys. Lett. 105 (2014), 231905.

[50] Y. Imade, V.E. Gusev, O. Matsuda, M. Tomoda, P.H. Otsuka, O.B. Wright, Gigahertz optomechanical photon–phonon transduction between nanostructure lines, Nano Lett. 21 (2021) 6261–6267.

[51] J. Higuet, T. Valier-Brasier, T. Dehoux, B. Audoin, Beam distortion detection and deflectometry measurements of gigahertz surface acoustic waves, Rev. Sci. Instrum. 82 (2011), 114905.

[52] D.H. Hurley, O.B. Wright, O. Matsuda, T. Suzuki, S. Tamura, Y. Sugawara, Time-resolved surface acoustic wave propagation across a single grain boundary, Phys. Rev. B 73 (2006), 125403.

[53] I.A. Veres, D.M. Profunser, A.A. Maznev, A.G. Every, O. Matsuda, O.B. Wright, Point source in a phononic grating: stop bands give rise to phonon-focusing caustics, New J. Phys. 14 (2012), 123015.

[54] B. Bonello, L. Belliard, J. Pierre, J.O. Vasseur, B. Perrin, O. Boyko, Negative refraction of surface acoustic waves in the subgigahertz range, Phys. Rev. B 82 (2010), 104109.

[55] P.H. Otsuka, K. Nanri, O. Matsuda, M. Tomoda, D.M. Profunser, I.A. Veres, S. Danworaphong, A. Khelif, S. Benchabane, V. Laude, O.B. Wright, Broadband evolution of phononic-crystal-waveguide eigenstates in real- and k-spaces, Sci. Rep. 3 (2013) 3351.

[56] H. Zhang, A. Antoncecchi, S. Edward, P. Planken, S. Witte, Ultrafast laser-induced guided elastic waves in a freestanding aluminum membrane, Phys. Rev. B 103 (2021), 064303.

[57] A. Abbas, Y. Guillet, J.M. Rampnoux, P. Rigail, E. Mottay, B. Audoin, S. Dilhaire, Picosecond time resolved opto-acoustic imaging with 48 MHz frequency resolution, Opt. Express 22 (2014) 7831–7843.

[58] Q. Xie, S. Mezil, P.H. Otsuka, M. Tomoda, J. Laurent, O. Matsuda, Z. Shen, O. B. Wright, Imaging gigahertz zero-group-velocity Lamb waves, Nat. Commun. 10 (2019) 2228.

[59] J.A. Rogers, A.A. Maznev, M.J. Banet, K.A. Nelson, Optical generation and characterization of acoustic waves in thin films: fundamentals and applications, Annu. Rev. Mater. Sci. 30 (1) (2000) 117–157.

[60] S. Mezil, K. Fujita, P.H. Otsuka, M. Tomoda, M. Clark, O.B. Wright, Active chiral control of GHz acoustic whispering-gallery modes, Appl. Phys. Lett. 111 (2017), 144103.

[61] M. Kouyate, T. Pezeril, D. Mounier, V. Gusev, Generation of inhomogeneous plane shear acoustic modes by laser-induced thermoelastic gratings at the interface of transparent and opaque solids, J. Appl. Phys. 110 (12) (2011), 123526.

[62] A. Vertikov, M. Kuball, A.V. Nurmikko, H.J. Maris, Time-resolved pump-probe experiments with subwavelength lateral resolution, Appl. Phys. Lett. 69 (1996) 2465–2467.

[63] T. Bienville, L. Belliard, P. Siry, B. Perrin, Photothermal experiments in the time and frequency domains using an optical near field microscope, Superlattices Microstruct. 35 (2004) 363–374.

[64] T.A. Klar, E. Engel, S.W. Hell, Breaking Abbé's diffraction resolution limit in fluorescence microscopy with stimulated emission depletion beams of various shapes, Phys. Rev. E 64 (2001), 066613.

[65] K.-H. Lin, C.-M. Lai, C.-C. Pan, J.-I. Chyi, J.-W. Shi, S.-Z. Sun, C.-F. Chang, C.-K. Sun, Spatial manipulation of nanoacoustic waves with nanoscale spot sizes, Nat. Nanotechnol. 2 (2007) 704–708.

[66] A. Crut, P. Maioli, N. Del Fatti, F. Vallée, Optical absorption and scattering spectroscopies of single nano-objects, Chem. Soc. Rev. 43 (2014) 3921.

[67] J.-F. Robillard, A. Devos, I. Roch-Jeune, P.A. Mante, Collective acoustic modes in various two-dimensional crystals by ultrafast acoustics: theory and experiment, Phys. Rev. B 78 (2008), 064302.

[68] B. Bonello, A. Ajinou, V. Richard, Ph. Djemia, S. M. Chérif, Surface acoustic waves in the GHz range generated by periodically patterned metallic stripes illuminated by an ultrashort laser pulse, J. Acous. Soc. Am. 110 (2001) 1943.

[69] C. Jean, L. Belliard, T.W. Cornelius, O. Thomas, Y. Pennec, M. Cassinelli, M. E. Toimil-Molares, B. Perrin, Spatiotemporal imaging of the acoustic field emitted by a single copper nanowire, Nano Lett. 16 (2016) 6592–6598.

[70] F. Xu, Y. Guillet, S. Ravaine, B. Audoin, All-optical in-depth detection of the acoustic wave emitted by a single gold nanorod, Phys. Rev. B 97 (2018), 165412.

[71] O. Matsuda, M.C. Larciprete, R. Li Voti, O.B. Wright, Fundamentals of picosecond laser ultrasonics, Ultrasonics 56 (2015) 3–20.

[72] V.E. Gusev, P. Ruello, Advances in applications of time-domain Brillouin scattering for nanoscale imaging, Appl. Phys. Rev. 5 (2018), 031101.

[73] J.-P. Monchalin, Optical detection of ultrasound, IEEE Trans. Ultras. Ferroelec. Freq. Contr. UFFC-33 33 (5) (1986) 485.

[74] D. Royer, E. Dieulesaint, Optical detection of sub-Angstrom transient mechanical displacement, IEEE Ultrason. Symp. Proc. (1986) 527–530.

[75] H.-N. Lin, R.J. Stoner, H.J. Maris, J. Tauc, Phonon attenuation and velocity measurements in transparent materials by picosecond acoustic interferometry, J. Appl. Phys. 69 (7) (1991) 3816–3822.

[76] S. Kashiwada, O. Matsuda, J.J. Baumberg, R. Li Voti, O.B. Wright, In situ monitoring of the growth of ice films by laser picosecond acoustics, J. Appl. Phys. 100 (7) (2006), 073506.

[77] M.-F. Ponge, L. Liu, C. Aristégui, B. Audoin, Scattering of GHz coherent acoustic phonons by silica nanoparticles in probed with the time-domain Brillouin spectroscopy, Appl. Phys. Lett. 115 (2019), 133101.

[78] J. Pupeikis, B. Willenberg, F. Bruno, M. Hettich, A. Nussbaum-Lapping, M. Golling, C.P. Bauer, S.L. Camenzind, A. Benayad, P. Camy, B. Audoin, C. R. Phillips, U. Keller, Picosecond ultrasonics with a free-running dual-comb laser, Opt. Express 29 (22) (2021) 35735–35754.

[79] A. Devos, Colored ultrafast acoustics: from fundamentals to applications, Ultrasonics 56 (2015) 90–97.

[80] O.B. Wright, Thickness and sound velocity measurement in thin transparent films with laser picosecond acoustics, J. Appl. Phys. 71 (1992) 1617–1629.

[81] C. Rossignol, B. Perrin, S. Laborde, L. Vandenbulcke, M.I. De Barros, P. Djemia, Nondestructive evaluation of micrometric diamond films with an interferometric picosecond ultrasonics technique, J. Appl. Phys. 95 (8) (2004) 4157–4162.

[82] O. Matsuda, O.B. Wright, Reflection and transmission of light in multilayer perturbed by picosecond strain pulse propagation, J. Opt. Soc. Am. B 19 (2002) 3028–3040.

[83] C. Rossignol, B. Perrin, B. Bonello, P. Djemia, P. Moch, H. Hurdequint, Elastic properties of ultrathin permalloy/alumina multilayer films using picosecond ultrasonics and Brillouin light scattering, Phys. Rev. B 70 (2004), 094102.

[84] M. Tomoda, O. Matsuda, O.B. Wright, R. Li Voti, Tomographic reconstruction of picosecond acoustic strain propagation, Appl. Phys. Lett. 90 (2007), 041114.

[85] O. Matsuda, O.B. Wright, Laser picosecond acoustics in a two-layer structure with oblique probe light incidence, Ultrasonics 42 (2004) 653–656.

[86] T. Dehoux, N. Chigarev, C. Rossignol, B. Audoin, Three-dimensional elasto-optical interaction for reflectometric detection of diffracted acoustic fields in picosecond ultrasonics, Phys. Rev. B 76 (2007), 024311.

[87] O. Matsuda, O.B. Wright, D.H. Hurley, V. Gusev, K. Shimizu, Coherent shear phonon generation and detection with picosecond laser acoustics, Phys. Rev. B 77 (2008), 224110.

[88] D. Mounier, E. Morozov, P. Ruello, J.-M. Breteau, P. Picart, V. Gusev, Detection of shear picosecond acoustic pulses by transient femtosecond polarimetry, Eur. Phys. J. 153 (2008) 243–246.

[89] O. Matsuda, M. Tomoda, T. Tachizaki, S. Koiwa, A. Ono, K. Aoki, R.P. Beardsley, O.B. Wright, Ultrafast ellipsometric interferometry for direct detection of coherent phonon strain pulse profiles, J. Opt. Soc. Am. B 30 (7) (2013) 1911–1921.

[90] J.-M. Halbout, C.L. Tang, Femtosecond interferometry for nonlinear optics, Appl. Phys. Lett. 40 (1982) 765–767.

[91] B. Perrin, B. Bonello, J.-C. Jeannet, E. Romatet, Interferometric detection of hypersound waves in modulated structures, Prog. Nat. Sci. S6 (1996) 444.

[92] H. Hurley, O.B. Wright, Detection of ultrafast phenomena by use of a modified Sagnac interferometer, Opt. Lett. 24 (1999) 1305.

[93] F. Decremps, L. Belliard, B. Perrin, M. Gauthier, Sound velocity and absorption measurements under high pressure using picosecond ultrasonics in a diamond anvil cell: application to the stability study of AlPdMn, Phys. Rev. Lett. 100 (2008), 035502.

[94] M. Nikoonahad, S. Lee, H. Wang, Picosecond photoacoustics using common-path interferometry, Appl. Phys. Lett. 76 (2000) 514.

[95] J.-Y. Duquesne, B. Perrin, Ultrasonic attenuation in a quasicrystal studied by picosecond acoustics as a function of temperature and frequency, Phys. Rev. B 68 (2003), 134205.

[96] M.A. Van Dijk, M. Lippitz, D. Stolwijk, M. Orrit, A common-path interferometer for time-resolved and shot-noise-limited detection of single nanoparticles, Opt. Express 15 (5) (2007) 2273–2287.

[97] J. Chandezon, J.-M. Rampnoux, S. Dilhaire, B. Audoin, Y. Guillet, In-line femtosecond common-path interferometer in reflection mode, Opt. Express 23 (21) (2015) 27011.

[98] L. Liu, Y. Guillet, B. Audoin, Common-path conoscopic interferometry for enhanced picosecond ultrasound detection, J. Appl. Phys. 123 (17) (2018), 173103.

[99] Y. Li, Q. Miao, A.V. Nurmikko, H.J. Maris, Picosecond ultrasonic measurements using an optical cavity, J. Appl. Phys. 105 (8) (2009), 083516.

[100] A. Bartels, F. Hudert, C. Janke, T. Dekorsy, K. Kohler, Femtosecond time-resolved optical pump-probe spectroscopy at kilohertz-scan-rates over nanosecond-time-delays without mechanical delay line, Appl. Phys. Lett. 88 (4) (2006), 041117.

[101] S. Dilhaire, G. Pernot, G. Calbris, J.M. Rampnoux, S. Grauby, Heterodyne picosecond thermoreflectance applied to nanoscale thermal metrology, J. Appl. Phys. 110 (11) (2011), 114314.

[102] A. Bruchhausen, J. Lloyd-Hughes, M. Hettich, R. Gebs, M. Grossmann, O. Ristow, A. Bartels, M. Fischer, M. Beck, G. Scalari, J. Faist, A. Rudra, P. Gallo, E. Kapon, T. Dekorsy, Investigation of coherent acoustic phonons in terahertz quantum

cascade laser structures using femtosecond pump-probe spectroscopy, J. Appl. Phys. 112 (2012), 033517.
[103] R. Gebs, G. Klatt, C. Janke, T. Dekorsy, A. Bartels, High-speed asynchronous optical sampling with sub-50 fs time resolution, Opt. Express 18 (2010) 5974–5983.
[104] Y. Ezzahri, S. Grauby, J.M. Rampnoux, H. Michel, G. Pernot, W. Claeys, S. Dilhaire, C. Rossignol, G. Zeng, A. Shakouri, Coherent phonons in Si/SiGe superlattices, Phys. Rev. B 75 (19) (2007), 195309.
[105] S.M. Link, A. Klenner, M. Mangold, C.A. Zaugg, M. Golling, B.W. Tilma, U. Keller, Dual-comb modelocked laser, Opt. Express 23 (5) (2015) 5521.
[106] C.J. Morath, H.J. Maris, Phonon attenuation in amorphous solids studied by picosecond ultrasonics, Phys. Rev. B 54 (1) (1996) 203–213.
[107] J.D. Choi, T. Feurer, M. Yamaguchi, B. Paxton, K.A. Nelson, Generation of ultrahigh-frequency tunable acoustic waves, Appl. Phys. Lett. 87 (8) (2005), 081907.
[108] C. Klieber, E. Peronne, K. Katayama, J. Choi, M. Yamaguchi, T. Pezeril, K. A. Nelson, Narrow-band acoustic attenuation measurements in vitreous silica at frequencies between 20 and 400 GHz, Appl. Phys. Lett. 98 (21) (2011), 211908.
[109] A. Bruchhausen, R. Gebs, F. Hudert, D. Issenmann, G. Klatt, A. Bartels, O. Schecker, R. Waitz, A. Erbe, E. Scheer, J.R. Huntzinger, A. Mlayah, T. Dekorsy, Subharmonic resonant optical excitation of confined acoustic modes in a free-standing semiconductor membrane at GHz frequencies with a high-repetition-rate femtosecond laser, Phys. Rev. Lett. 106 (2011), 077401.
[110] S. Kaneko, M. Tomoda, O. Matsuda, A method for the frequency control in time-resolved two-dimensional gigahertz surface acoustic wave imaging, AIP Adv. 111 (4) (2017), 144103.
[111] P. Ahn, Z. Zhang, C. Sun, O. Balogun, Ultrasonic near-field optical microscopy using a plasmonic nanofocusing probe, J. Appl. Phys. 113 (23) (2013), 234903.
[112] Q. Li, K. Hoogeboom-Pot, D. Nardi, M.M. Murnane, H.C. Kapteyn, M.E. Siemens, E.H. Anderson, O. Hellwig, E. Dobisz, B. Gurney, R. Yang, K.A. Nelson, Generation and control of ultrashort-wavelength two-dimensional surface acoustic waves at nanoscale interfaces, Phys. Rev. B 85 (2012), 195431.
[113] J. Hernandez-Charpak, K. Hoogeboom-Pot, Q. Li, T. Frazer, J. Knobloch, M. Tripp, S. King, E. Anderson, W. Chao, M. Murnane, D. Nardi, Full characterization of the mechanical properties of 11–50 nm ultrathin films: influence of network connectivity on the Poisson's ratio, Nano Lett. 17 (2017) 2178–2183.
[114] R. Berte, F. Della Picca, M. Poblet, Y. Li, E. Cortés, R.V. Craster, S.A. Maier, A. V. Bragas, Acoustic far-field hypersonic surface wave detection with single plasmonic nanoantennas, Phys. Rev. Lett. 121 (2018), 253902.
[115] J. Gargiulo, I.L. Violi, S. Cerrota, L. Chvátal, E. Cortés, E.M. Perassi, F. Diaz, P. Zemánek, F.D. Stefani, Accuracy and mechanistic details of optical printing of single Au and Ag nanoparticles, ACS Nano 11 (2017) 9678–9688.
[116] Y. Tian, P. Navarro, M. Orrit, Single molecule as a local acoustic detector for mechanical oscillators, Phys. Rev. Lett. 113 (2014), 135505.
[117] T. Dehoux, M. Abi Ghanem, O. Zouani, M. Ducousso, N. Chigarev, C. Rossignol, N. Tsapis, M.-C. Durrieu, B. Audoin, Probing single-cell mechanics with picosecond ultrasonics, Ultrasonics 56 (2015) 160–171.
[118] A. Viel, E. Péronne, O. Sénépart, L. Becerra, C. Legay, F. Semprez, L. Trichet, T. Coradin, A. Hamraoui, L. Belliard, Picosecond ultrasounds as elasticity probes in neuron-like cells models, Appl. Phys. Lett.. 11 (21) (2019), 213701.
[119] F. Bruno, L. Saint-Martin, D. Thuau, B. Audoin, Multilayer transducer for highly efficient initiation of time-resolved Brillouin scattering, Appl. Phys. Lett. 120 (2022), 212201.
[120] F. Pérez-Cota, R.J. Smith, E. Moradi, L. Marques, K.F. Webb, M. Clark, Thin-film optoacoustic transducers for subcellular Brillouin oscillation imaging of individual biological cells, Appl. Opt. 54 (28) (2015) 8388.
[121] The refractive index and mass density for cell are typically n = 1.35 and ρ=1.1g. cm^{-3}.
[122] L. Liu, A. Viel, G. Le Saux, L. Plawinski, G. Muggiolu, P. Barberet, M. Pereira, C. Ayela, H. Seznec, M.-C. Durrieu, J.-M. Olive, B. Audoin, Remote imaging of single cell 3D morphology with ultrafast coherent phonons and their resonance harmonics, Sci. Rep. 9 (2019) 6409.
[123] L. Liu, L. Plawinski, M.-C. Durrieu, B. Audoin, Label-free multi-parametric imaging of single cells: dual picosecond optoacoustic microscopy, J. Biophotonics 12 (8) (2019), e201900045.
[124] S. Danworaphong, M. Tomoda, Y. Matsumoto, O. Matsuda, T. Ohashi, H. Watanabe, M. Nagayama, K. Gohara, P. Otsuka, O.B. Wright, Three-dimensional imaging of biological cells with picosecond ultrasonics, Appl. Phys. Lett. 106 (16) (2015), 163701.
[125] R.J. Smith, F. Pérez-Cota, L. Marques, M. Clark, 3D phonon microscopy with sub-micron axial resolution, Sci. Rep. 11 (2021) 3301.
[126] F. Pérez-Cota, R.J. Smith, E. Moradi, L. Marques, K.F. Webb, M. Clark, High resolution 3D imaging of living cells with sub-optical wavelength phonons, Sci. Rep. 6 (2016) 39326.
[127] T. Dehoux, M. Abi Ghanem, O.F. Zouani, J.-M. Rampnoux, Y. Guillet, S. Dilhaire, M.-C. Durrieu, B. Audoin, All-optical broadband ultrasonography of single cells, Sci. Rep. 5 (2015) 1038.
[128] H.G. Tattersall, The ultrasonic pulse-echo technique as applied to adhesion testing, J. Phys. D Appl. Phys. 6 (1973) 819.
[129] M. Abi Ghanem, T. Dehoux, O.F. Zouani, A. Gadalla, M.-C. Durrieu, B. Audoin, Remote opto-acoustic probing of single-cell adhesion on metallic surfaces, J. Biophotonics 7 (6) (2014) 453–459.
[130] A. Hamraoui, O. Senepart, M. Schneider, S. Malaquin, E. Peronne, L. Becerra, F. Semprez, C. Legay, L. Belliard, Correlative imaging of motoneuronal cell elasticity by pump and probe spectroscopy, Biophys. J. 120 (3) (2021) 402–408.
[131] Y. Sung, W. Choi, N. Lue, R.R. Dasari, Z. Yaqoob, Stain-free quantification of chromosomes in live cells using regularized tomographic phase microscopy, PLoS One 7 (2012), e49502.
[132] P.D. Antonio, M. Lasalvia, G. Perna, V. Capozzi, Scale-independent roughness value of cell membranes studied by means of AFM technique, Biochim. Biophys. Acta 2012 (1818) 3141.
[133] Y.H. Wang, C.X. Xu, N.C. Jiang, L.Q. Zheng, J.S. Zeng, C.M. Qiu, H.Q. Yang, S. S. Xie, Quantitative analysis of the cell-surface roughness and viscoelasticity for breast cancer cells discrimination using atomic force microscopy, Scanning 38 (6) (2016) 558.
[134] G.N. Papanicolaou, H.F. Traut, The diagnostic value of vaginal smears in carcinoma of the uterus, Am. J. Obstet. Gynecol. 42 (1941) 193–206.
[135] B. Ladoux, A. Nicolas, Physically based principles of cell adhesion mechanosensitivity in tissues, Rep. Prog. Phys. 75 (11) (2012), 116601.
[136] O.F. Zouani, C. Chanseau, B. Brouillaud, R. Bareille, F. Deliane, M.-P. Foulc, A. Mehdi, M.-C. Durrieu, Altered nanofeature size dictates stem cell differentiation, J. Cell Sci. 125 (5) (2012) 1217–1224.
[137] C. Zhu, G. Bao, N. Wang, Cell mechanics: mechanical response, cell adhesion, and molecular deformation, Annu. Rev. Biomed. Eng. 02 (2000) 189–226.
[138] P. Kanchanawong, G. Shtengel, A.M. Pasapera, E.B. Ramko, M.W. Davidson, H. F. Hess, C.M. Waterman, Nanoscale architecture of integrin-based cell adhesions, Nature 468 (2010) 580–584.
[139] E. Peronne, O. Senepart, C. Legay, F. Semprez, A. Hamraoui, L. Belliard, Data-clustering analysis of scanning ultrafast acoustic experiments: revealing acoustic and structural properties of a motoneuron, Phys. Rev. Appl. 18 (2022), 034051.
[140] M. Abi Ghanem, T. Dehoux, L. Liu, G. Le Saux, L. Plawinski, M.-C. Durrieu, B. Audoin, Opto-acoustic microscopy reveals adhesion mechanics of single cells, Rev. Sci. Instrum. 89 (1) (2018), 014901.
[141] M. Zwerger, C.Y. Ho, J. Lammerdin, Nuclear mechanics in disease, Annu. Rev. Biomed. Eng. 13 (1) (2011) 397–428.
[142] J.D. Pajerowski, K.N. Dahl, F.L. Zhong, P. Zammak, D.E. Discher, Physical plasticity of the nucleus in stem cell differentiation, Proc. Natl. Acad. Sci. 104(40) (2007) 15619–15624.
[143] Y. Xia, C.R. Pfeifer, S. Cho, D.E. Discher, J. Irianto, Nuclear mechanosensing, Emerg. Top Life Sci. 2 (5) (2018) 713–725.
[144] H. Strickfaden, T.O. Tolsma, A. Sharma, D.A. Underhill, J.C. Hansen, M. J. Hendzel, Condensed chromatin behaves like a solid on the mesoscale in vitro and in living cells, Cell 183 (2020) 1772–1784.
[145] O.F. Zouani, T. Dehoux, M.-C. Durrieu, B. Audoin, Universality of the network-dynamics of the cell nucleus at high frequencies, Soft Matter 10 (2014) 8737.
[146] K. Saha, A.J. Keung, E.W. Irwin, Y. Li, L. Little, D.V. Schaffer, K.E. Healy, Substrate modulus directs neural stem cell behavior, Biophys. J. 95 (9) (2008) 4426.
[147] R. Mc Beath, D.M. Pirone, C.M. Nelson, K. Bhadriraju, C.S. Chen, Cell shape, cytoskeletal tension, and RhoA regulate stem cell lineage commitment, Dev. Cell 6 (4) (2004) 483.
[148] N. Wang, J.D. Tytell, D.E. Ingber, Mechanotransduction at a distance: mechanically coupling the extracellular matrix with the nucleus, Cell Biol. 10 (2009) 75.
[149] A. Tajik, Y. Zhang, F. Wei, J. Sun, Q. Jia, W. Zhou, R. Singh, N. Khanna, A. S. Belmont, N. Wang, Transcription upregulation via force-induced direct stretching of chromatin, Nat. Mater. 15 (2016) 1287.
[150] F. Pérez-Cota, R. Fuentes-Domínguez, S. La Cavera, W. Hardiman, M. Yao, K. Setchfield, E. Moradi, S. Naznin, A. Wright, K.F. Webb, A. Huett, C. Friel, V. Sottile, H.M. Elsheikha, R.J. Smith, M. Clark, Picosecond ultrasonics for elasticity-based imaging and characterization of biological cells, J. Appl. Phys. 12 (16) (2020), 160902.
[151] J. Zhang, F. Alisafaei, M. Nikolić, X.A. Nou, H. Kim, V.B. Shenoy, G. Scarcelli, Nuclear mechanics within intact cells is regulated by cytoskeletal network and internal nanostructures, Small 16 (18) (2020) 1907688.
[152] S.P. Jackson, J. Bartek, The DNA-damage response in human biology and disease, Nature 461 (2009) 1071–1078.
[153] T. Helleday, J. Lo, D.C. van Gent, B.P. Engelward, DNA double-strand break repair: from mechanistic understanding to cancer treatment, DNA Repair 6 (2007) 923–935.
[154] S. Herbert, A. Brion, J.-M. Arbona, M. Lelek, A. Veillet, B. Lelandais, J. Parmar, F. G. Fernández, E. Almayrac, Y. Khalil, E. Birgy, E. Fabre, C. Zimmer, Chromatin stiffening underlies enhanced locus mobility after DNA damage in budding yeast, EMBO J. 36 (17) (2017) 2595–2608.
[155] A. Dos Santos, A.W. Cook, R.E. Gough, M. Schilling, N.A. Olszok, I. Brown, L. Wang, J. Aaron, M.L. Martin-Fernandez, F. Rehfeldt, C.P. Toseland, DNA damage alters nuclear mechanics through chromatin reorganization, Nucleic Acids Res. 49 (1) (2021) 340–353.
[156] L. Liu, M. Simon, G. Muggiolu, F. Vilotte, M. Antoine, J. Caron, G. Kantor, P. Barberet, H. Seznec, B. Audoin, Changes in intra-nuclear mechanics in response to DNA damaging agents revealed by time-domain Brillouin micro-spectroscopy, Photoacoustics 27 (2022), 100385.

Bertrand Audoin is Professor at Université de Bordeaux, France. He was involved in laser ultrasonics and their applications to the non-destructive evaluation of anisotropic materials. The researches led in his group also focused on picosecond ultrasonics. They have performed the acoustic diffraction in sub-micron sized solid samples and used absorption by a single particle as a opto-acoustic source. His current research focus on picosecond biophononics: B. Audoin has demonstrated the first applications of picosecond ultrasonics to biologic media, a field totally unexplored at that time. His group has developed the opto-

acoustic microscopy of single cells, an imaging modality where the mechanical properties is the contrast mechanism.